T-2404

A MÖSSBAUER STUDY OF THE TRANSFORMATIONS OF THE IRON MINERALS IN OIL SHALE DURING RETORTING

by

Daniel Carl Melchior III

ProQuest LLC.
789 East Eisenhower Parkway
P.O. Box 1346
Ann Arbor, MI 48106 – 1346

T-2404

A thesis submitted to the Faculty and the Board of Trustees of the Colorado School of Mines in partial ful fillment of the requirements for the degree of Master of Science (Geochemistry)

Golden, Colorado

Date 11/25/80

Signed: Daniel C. Melchior III

Daniel Carl Melchior III

Approved: Thomas Wildeman

Dr. Thomas R. Wildeman
Thesis Advisor

Golden, Colorado

Date 11/25/80

George H Kennedy

Dr. George H. Kennedy
Head of Department
Chemistry/Geochemistry

ABSTRACT

Iron phases in raw and retorted shales have been studied from the TOSCO II, Paraho, and Lawrence Livermore Laboratory (LLL) 125 kg retorting processes by Mössbauer effect spectroscopy. Using the Mössbauer effect, changes in the iron mineralogy during retorting were followed. Results show that the pyrite fraction in the TOSCO II, and LLL hydrogen run S-9 samples underwent changes during retorting while the iron-containing carbonates did not As in other pyrolysis processes, FeS_2 breakdown is affected by the presence of organic matter. Hydrogen released by the indigenous kerogen acts to reduce pyrite to the magnetic sulfide pyrrhotite. In all of the retorts containing oxygen, carbonate breakdown was observed prior to pyrite oxidation. Free oxygen is introduced to several retorts. The iron minerals within these systems eventually become a mixture of the oxides hematite and magnetite. The occurrence of these oxides versus other phases reflects distinct temperatures and oxygen fugacities within the system. This study demonstrates that alteration of specific iron minerals during retorting may be controlled by varying the internal retorting conditions

TABLE OF CONTENTS

LIST OF FIGURES

LIST OF TABLES

ACKNOWLEDGEMENTS

I would like to express my sincere appreciation to Dr. T R. Wildeman for serving as my thesis advisor. I would also like to thank both Dr. Wildeman and Dr D. L. Williamson for all their assistance throughout A tremendous wealth of knowledge has been accrued by me throughout this project from these gentlemen, for which I am truly indebted. I am also grateful to Dr J. Giulianelli for serving as a committee member. Special thanks must go to my family for their constant concern.

I would also like to thank the faculties at the Colorado School of Mines and the Southeastern Massachusetts University for their help throughout my scientific career.

This study has been partially funded by DOE grant EV-102-98.

INTRODUCTION

The Green River formation in Colorado, Wyoming, and Utah is well known for its hydrocarbon content and unique assemblage of minerals. Extraction of the organic compounds from oil shale on a large scale basis is accomplished by retorting. The process of retorting involves thermal separation of the organic matter from the rock matrix.

Development of the potential resources of the Green River formation has posed numerous questions involving the environment. Questions concerning element mobility and speciation have been approached by several researchers (1, 2, 3, 4). Some have linked the mobility of toxic elements to the sulfide minerals of which pyrite is dominant (1, 5). For this reason a study of the speciation of the iron phases in raw and retorted shales warrants attention.

The mineralogy of shale in the Green River formation has been investigated by various techniques (6, 7). Mössbauer spectroscopy has recently been applied in studying the mineralogic speciation of iron within unretorted shales and marlstones by Cole and others (8). In the paper by Cole, seven iron-bearing minerals were identified in oil shale of the Green River formation. The seven minerals may be distinguished as belonging to two distinct mineralogi

cal groups, carbonates and sulfides. Iron in sulfides existed as pyrite, pyrrhotite, and marcasite, and in the carbonates as siderite, ankerite, and dolomite.

The mineral assemblages present in a shale are also known to influence its retorting characteristics (9, 10) As a shale is exposed to heating, the mineral assemblages are subject to changes. The minerals are susceptible to decomposition, degradation, oxidation, or reduction during exposure to high temperatures and various redox conditions (10, 11, 13)

Retorting processes in use today can be categorized into four groups: 1) above ground, direct combustion mode (DC), 2) above ground, indirect heating (IH), 3) below ground, modified in-situ (MIS), and 4) in-situ retorting. In this paper, three retort types plus a laboratory model have been studied: 1) (DC) Paraho, 2) (IH) TOSCO II, 3) (MIS) Lawrence Livermore Laboratory 125 kg retort, and the Fischer Assay laboratory model. The fate of the indigenous iron minerals during retorting under three different methods, temperatures, and redox conditions is the objective of this study.

TECHNIQUES AND PROCEDURES

The shales used in this study were obtained from several sources. The TOSCO II samples (OS-1, SS-2, and the Fischer Assay process) were donated by Dr. T.R. Wildeman (12) Dr. Wildeman and R. Heistand donated splits from the Paraho system (13) (an unretorted feedstock, a spent shale, plus a dust from the Paraho baghouse) Dr. J.P. Fox of the Lawrence Berkeley laboratories made available samples from their 125 kg modified in-situ retort (1) All specimens were sampled and prepared in the manner outlined by Wildeman (14) The sampling of the spent shales from the retorts is described in Wildeman (12, 13), Wildeman and Heistand (13), and Fox (1)

The TOSCO II retort indirectly heats the shale via heated ceramic balls This process provides a uniform heat flow to the feedstock and simultaneously grinds the shale (2) The Paraho process involves direct combustion of residual carbon on previously retorted shale to supply the retort heat. The temperature is controlled by feeding gases through ports in the vessel (15) The Lawrence Livermore Laboratory's 125 kg retort is a modified in-situ process. In this study it is operated by introducing indirectly heated gas (16) Table 1 lists the samples studied and their retorting conditions

Table 1: RETORTED SAMPLES AND RETORTING CONDITIONS.

Name	Type	Heating	Max. Temp	Atmosphere	Reference
TOSCO 11	Surface	Indirect	482°C	Pyrolysis Gases	2
Fischer Assay	Laboratory	Indirect	500	Pyrolysis Gases	17
Paraho	Surface	Direct	600	Air + Combustion Derived CO_2	15
Lawrence Livermore Laboratory 125 Kg	Modified In-situ	Indirect			
	S-7	Indirect	750	Air + N_2 (7.6% O_2)	1
	S-9	Indirect	510	H_2	1
	S-10	Indirect	935	Air + Recycled Gases (10.5% O_2)	1
	S-11B	Indirect	1030	Air + Recycled Gases (21% O_2)	1

Mössbauer analysis was performed using a conventional constant acceleration spectrometer. An absorber was made from each oil shale listed in Table 1 by compressing one gram of material into a disk 2.54 cm in diameter. Duplicate absorbers and duplicate runs were made for some of the shales to test reproducibility. Several measurements were made at below ambient temperatures in a commercial cryostat. One sample was encapsulated in a graphite cell and run at elevated temperatures in a commercial vacuum furnace. Velocity calibrations were carried out with an iron foil and all Mössbauer isomer shifts reported here are with respect to α-Fe at room temperature. The spectra obtained were each deconvoluted with a computer program based on a least squares Lorentzian algorithm. The Mössbauer parameters determined from the fits included the isomer shift (δ), quadrupole splitting (Δ), magnetic hyperfine field (H), and the effective thickness for each iron-containing compound. The values of the quadrupole splitting of magnetic components reported in this paper are calculated from the velocity positions of the four outer lines of the six line resonance as $\Delta = [(V_6 - V_5) \quad (V_2 - V_1)]/2$. V_1 is the lowest velocity position and V_6 is the highest.

The calculations of relative percentages of Fe as different species of this study were performed following

the determination that the recoilless fractions of the phases observed were equal This determination was made by running a shale absorber at ambient temperature and then at 76K to observe the relative resonance amounts of each species. The results show that within the limits of the errors this assumption is valid. Therefore, the ratio of the effective thickness of each specie to the total effective thickness of the sample gives the fractional amount of iron present as that mineral

RESULTS

Figures 2 through 26 give the spectra of each run.

Table 2 summarizes the iron mineral phases identified in each sample. Duplicate absorbers and runs have shown that the method of analysis is reproducible. The numbers listed in Table 2 include Mössbauer parameters derived from each spectrum, percentages of iron as that species, plus the mineralogic name assigned to each component based on comparison of these Mössbauer parameters to literature values. Experimental uncertainties in the last digit are given in parentheses after that digit and represent an estimated error based on counting statistics plus errors arising due to computer deconvolution of overlapping resonance lines. Blank spaces in Table 2 are present where the Mössbauer parameters could not be determined due to overlapping resonance of one of the lines

Table 2. MÖSSBAUER ANALYSIS RESULTS

Sample	δ(mm/sec)	Δ(mm/sec)	H (kOe)	% Fe	Mineral
OS-1	0.40(1)	0.63(1)		42(3)	Pyrite
T=76K	1.38(1)	2.41(1)		21(3)	Siderite
	1.37(1)	1.97(1)		37(3)	Ankerite
OS-1	0.32(1)	0.61(1)		39(3)	Pyrite
T=301K	1.24(1)	1.86(1)		16(3)	Siderite
	1.24(1)	1.51(1)		45(3)	Ankerite
SS-2	0.60(8)	0.25(8)	271(2)	18(4)	Pyrrhotite
T=298K	1.23(1)	1.53(1)		40(5)	Ankerite
	1.20(3)	1.98(4)		11(5)	Siderite
	0.31(3)	0.7(1)		31(5)	Pyrite
Fischer Assay	0.91(3)	-0.08(3)	327(1)	24(5)	Pyrrhotite
T=76K	0.75(1.0)	0.41(7)	270(3)	10(5)	Pyrrhotite
				49(5)	Carbonate
				17(5)	Pyrite
Fischer Assay	0.60(6)	-0.02(2)	303(2)	18(4)	Pyrrhotite
T=302K	0.56(6)	0.17(4)	267(2)	20(4)	Pyrrhotite
				40(5)	Carbonate
				22(5)	Pyrite
Raw 1B	0.38(1)	0.65(1)		17(2)	Pyrite
T=76K	1.38(1)	1.91(1)		48(2)	Ankerite
(Center)	1.37(1)	2.32(1)		21(2)	Siderite
	1.28(1)	2.99(2)		9(2)	Illite
				5(2)	Troilite

Table 2. Continued

Sample	δ(mm/sec)	Δ(mm/sec)	H (kOe)	% Fe	Mineral
Raw 1B	0.31(1)	0.61(1)		20(3)	Pyrite
T=298K	1.24(1)	1.50(1)		50(3)	Ankerite
	1.23(1)	1.86(1)		17(3)	Siderite
	1.11(1)	2.70(1)		7(3)	Illite
	0.5(1)		312(4)	6(3)	Troilite
SOS-9	0.67(1)		308(2)	12(4)	Pyrrhotite
T=295K	0.75(1)		270(2)	13(4)	Pyrrhotite
	1.24(2)	1.51(2)		55(4)	Ankerite
	0.32(2)	0.60(2)		11(4)	Pyrite & Illite
	1.2(1)	2.0(2)		9(4)	Siderite
SOS-7	0.39(1)	-0.23(1)	514(2)	24(7)	Hematite
T=295K	0.3(1)	0.1(1)	444(4)	38(7)	Magnetite
				17(7)	Carbonate
				21(7)	Pyrite & Illite
SOS-10	0.48(3)	0.22(2)	535(2)	21(5)	Hematite
T=76K	0.38(2)	-0.01(2)	507(2)	67(5)	Magnetite
	0.00(3)			6(3)	Superparamagnetic
	0.89(3)			6(3)	Oxides
SOS-10	0.38(1)	-0.23(1)	513(2)	20(5)	Hematite
T=295K	0.28(2)	0.06(2)	435(2)	59(5)	Magnetite
	-0.10(3)			11(5)	Superparamagnetic
	0.81(3)			10(5)	Oxides

Table 2. Continued

Sample	δ(mm/sec)	Δ(mm/sec)	H (kOe)	% Fe	Mineral
SOS-11B	0.57(3)	0.12(2)	534(2)	26(4)	Hematite
T=6K	0.38(3)	-0.03(2)	512(2)	61(4)	Magnetite
	-0.01(3)			7(4)	Superparamagnetic
	0.92(3)			6(4)	Oxides
SOS-11B	0.46(2)	0.10(2)	529(3)	27(3)	Hematite
T=76K	0.37(2)	-0.02(1)	501(3)	53(3)	Magnetite
	-0.01(2)			11(3)	Superparamagnetic
	0.92(2)			9(3)	Oxides
SOS-11B	0.38(1)	-0.24(1)	514(2)	16(4)	Hematite
T=295K	0.30(3)	0.09(2)	431(2)	56(4)	Magnetite
	-0.10(1)			15(4)	Superparamagnetic
	0.81(1)			13(4)	Oxides
SOS-11B	0.25(3)	-0.22(3)	467(2)	16(3)	Hematite
T=491K	0.2(3)	0.2(2)	237(11)	37(8)	Magnetite
	-0.18(4)			22(3)	Magnetite & Hema-
	0.52(4)			25(3)	tite
SOS-11B	0.15(4)	-0.26(4)	416(2)	10(5)	Hematite
T=637K	0.34(1)			25(5)	Magnetite
	-0.23(1)			19(5)	Magnetite & Hema-
	0.4(1)			46(7)	tite
SOS-11B	0.00(4)	-0.26(4)	337(2)	12(10)	Hematite
T=773K	-0.29(1)			17(10)	Magnetite
	0.22(1)			23(10)	Magnetite & Hema-
	0.02(5)			48(10)	tite

Table 2. Continued

Sample	δ(mm/sec)	Δ(mm/sec)	H(kOe)	% Fe	Mineral
SOS-11B T=863K	-0.53(2) 0.15(2)				Magnetite & Hematite
Paraho Unretorted Shale	Refer RAW 1B				
Paraho Retorted T = 298K	0.59(6)	-0.22(5)	510(2)	25(5)	Hematite
	0.7(2)	0.22(7)	472(5)	19(5)	Magnetite
	1.24(3)	1.5(1)		36(10)	Carbonate
	0.34(3)	0.8(2)		16(10)	Pyrite & Illite
			277(10)	4(3)	Pyrrhotite
Paraho Baghouse Dust T=298K	0.28(3)	-0.01(3)	485(4)	7(5)	Magnetite
	0.65(5)	-0.2(1)	459(5)	40(5)	Magnetite
	0.37(4)	0.8(2)		23(9)	Pyrite & Illite
	1.24(2)	1.52(3)		30(9)	Carbonate

DISCUSSION

Analysis of the indigenous iron minerals within unretorted shales and marlstones was first attempted by Cole and others (8) In this study the iron mineralogy in oil shale is monitored prior to and subsequent to retorting. Table 1 is a list of the specific retorts studied while Table 2 shows the iron minerals found in this Mössbauer study.

Unretorted Shales

Unretorted shales that were investigated come from three processes. TOSCO OS-1 came from the Colony mine, and Paraho and Lawrence Livermore Raw 1B were mined at Anvil Points Raw 1B and the Paraho feedstock were sampled from the same locality at Anvil Points

From the initial spectra of the two samples it appears that their iron minerals are identical Consequently, special attention was paid to Raw 1B since several retorting runs were made using it as a feedstock. Detailed spectra were run on Raw 1B to fingerprint the minerals and it is assumed that conclusions drawn about Raw 1B may be extended to the Paraho feedstock. There is a distinct difference in the mineralogy between the Colony and Anvil Points shales

Mössbauer results show that there are four distinct mineralogic species present within Raw 1B: 1) a magnetic

iron sulfide, 2) an iron disulfide, 3) iron carbonates, and 4) an iron containing clay Table 2 displays the relative percentages of each mineral The true identification of the indigenous magnetic sulfide is rather difficult due to the limited quantity present; the Mössbauer parameters resemble those of the mineral troilite or pyrrhotite. The iron disulfide observed has parameters that match pyrite and not marcasite. Two different iron-containing carbonates observed were siderite and ankerite. The fourth iron-containing phase was also difficult to identify, however it does have parameters similar to a clay such as illite or chlorite. The identification of an iron-containing clay is not surprising since oil shale is a sedimentary rock.

OS-1 is distinctly different than Raw 1B in that only two iron containing mineralogic groups could be identified. In this sample, the minerals pyrite, siderite, and ankerite appeared in the resonance patterns

Aside from the measurements taken of OS-1 and Raw 1B at room temperature and 76K, one other measurement was attempted to verify if the mineral siderite was indeed present Siderite has been shown to exhibit a magnetic transition at 38K (18) For this reason, a measurement at 6K was taken to determine if a magnetic transition could be observed. Figure 5 displays the resonance patterns of

OS-1 at 6 and 76K. At 6K, the intensity of the carbonate peaks has significantly decreased. Two new peaks are observed that are split from the central resonance. This suggests that between 6 and 76K a magnetic transition has occurred. This piece of information, coupled with the other measurements, reinforces the presence of the mineral siderite within both OS-1 and Raw 1B.

Ankerite is an iron containing carbonate that has a structure similar to dolomite, but with larger cell parameters The increase in cell parameters is due to the partial replacement of Mg^{2+} by Fe^{2+} In the Mahogany zone of the Green River formation, ankerite is attributed as being the primary carbonate mineral (19) Smith and Robb (19) have reported an average formula of $Ca(Mg_{0.85}\ Fe_{0.15})(CO_3)_2$ for Mahogany zone ankerite. Mössbauer parameters for ankerite are documented and are similar to siderite (20) The values reported in this study resemble those previously reported A question arises as to whether the mineral observed here is "ankerite" or an impure dolomite. A search of the literature has revealed no data pertaining to variations in Mössbauer parameters as a function of ankerite/dolomite compositions For the purposes of this study the mineral will be referred to as ankerite.

Pyrite is a cubic mineral with the formula FeS_2; marcasite

is also FeS_2 however it is orthorhombic. Pyrrhotite is a magnetic sulfide that has a variety of compositions and is usually a monoclinic or hexagonal crystal (21) Mössbauer parameters for these minerals are well documented in the literature (22, 23) The parameters reported here for the disulfide are similar to those of pyrite with no significant amount of marcasite observed. Results for Raw 1B and the Paraho feedstock have revealed the presence of a magnetic mineral with a hyperfine field resembling that of troilite or pyrrhotite. The resonance attributed to this mineral is very small and not resolved to the point of positive identification. The magnetic splitting is larger than would be attributed as pyrrhotite and is about that of troilite. Therefore it has been denoted as troilite, the stoichiometric iron sulfide, and not pyrrhotite.

Retorted Shales

A prime concern of this work was to monitor the transformations that occur to oil shale when it is retorted. In all cases, the retorted shales are the retorted products of one of the three unretorted shales which were described in the previous section.

Two basic types of retorts were examined to compare how the internal conditions within the retort affect the iron species present in the retorted shale Three of the retorts

can be grouped in the category in which the shale is indirectly heated without air present Those retorts are the TOSCO II, Fischer Assay benchtop method, and the Lawrence Livermore Run S-9. For the remainder of runs from the Lawrence Livermore 125 kg modified in-situ retort, the feedstock was heated with oxygen present within the vessel The Paraho process uses direct combustion with oxygen to heat the shale. A distinct dichotomy exists between the transformations that occur in an indirect pyrolysis retort versus those retorts in which oxygen is present

Indirect heating retorts

Table 1 documents the atmosphere present during each retorting process In these retorts, oxygen is excluded and the shale is pyrolyzed. The transformations that occurred within each retort are consistent with what is observed in other pyrolysis processes, such as coal liquefaction (24) In each process, the mineral pyrrhotite was observed after retorting coupled with a reduction in the resonance attributed to the pyrite. The appearance of pyrrhotite in these retorted samples suggests that degradation of pyrite is responsible for its presence.

In the Fe-S phase system, large pyrite crystals are stable up to 1026K above which they incongruently melt to pyrrhotite and liquid sulfur (25) If, however, hydrogen

is present within a system containing pyrite, the pyrite will decompose at lower temperatures than if hydrogen is excluded (26) Within the pyrolysis type of retorts studied, the maximum temperature that was reached neighbored 773K. This temperature is far below the point at which pyrite alone will decompose. Indigenous hydrogen from the organic materials must react to reduce the pyrite.

The resonance patterns for SS-2, the Fischer Assay, and the LLL S-9 also reveal that the two carbonates remain unchanged during retorting. This is not unusual since the temperatures realized in the processing are far below the point where a significant amount of the carbonates would be expected to decompose (10) The fate of the clay in run S-9 is uncertain. Montano (27) has stated that, upon heating, such clays yield a resonance pattern that resembles pyrite due to the conversion of Fe^{2+} to the 3^{+} state. The iron within the clay observed in Raw 1B is in the 2^{+} state. The converted Fe^{3+} resonance resembles that of Fe(II) in pyrite and thus it was not possible to separate the resonance due to the clay from that pyrite.

The feedstock for S-9 (Raw 1B) also contained a small amount of a mineral that resembled troilite. Following retorting, no evidence existed that the troilite was still

present. Above 413K, troilite undergoes a solid state conversion to hexagonal pyrrhotite (25) The Mössbauer parameters of hexagonal pyrrhotite have been reported to be very similar to those of monoclinic pyrrhotite (28) It would be reasonable to assume that if hexagonal pyrrhotite did form from the original troilite, it would be accounted for in the total pyrrhotite resonance.

Oxygen containing retorts

As shown in Table 1, several systems were examined in which oxygen is present in the retort gases The Paraho process utilizes oxygen to directly combust carbon on the spent shale, while the modified in-situ process is heated indirectly and varies the internal gas compositions The feedstocks which entered both the Paraho and Lawrence Livermore Laboratory 125 kg retort have similar mineralogy This is discussed in the section titled "Unretorted Shales "

The results observed suggest that some oxidation of the original minerals is occurring. Run S-7 and the Paraho process results show similarities, with S-10 and S-11 continuing the trend of conversion of the original minerals to oxides In S-7 and Paraho, the maximum temperature has not exceeded 1023 and 873K respectively A large fraction of the iron carbonates have decomposed in these two retorts to oxides. It does appear that the indigenous pyrite has

remained unchanged during retorting. The possible contribution of an Fe^{3+} clay resonance to the pyrite resonance as discussed is questionable in this case. Under these conditions, formation of hematite or magnetite from the clay is also possible. If some of the pyrite has been decomposed, that fraction does not account for much of the original mineralogic percentage.

In runs S-10 and S-11 a complete conversion of the original minerals to oxides is observed. Several measurements were made on both S-10 and S-11 samples to characterize the components. Room temperature measurements revealed a large fraction of resonance that was suspected to be due to superparamagnetic particles To verify this, several spectra were obtained at several temperatures since it is well known that the superparamagnetic resonance can be temperature dependent (29) Both samples from S-10 and S-11 were run at 76K. The spectra revealed a smaller amount of superparamagnetic resonance and the resonance attributed to the oxides increased. The mineral hematite has been positively identified since the parameters obtained at 76K and 298K show that Morin transition has occurred between these temperatures. Magnetite is the other magnetic oxide formed during retorting. The identification of magnetite is based on parameters obtained at the various

temperatures plus the observance of a Verwey transition (30) between 298K and 76K. The relative intensities of the resonances corresponding to the octahedral and tetrahedral sites is not representative of pure bulk magnetite. This may be due to the presence of Ca^{2+} and Mg^{2+} impurities Figures 17, 18 and 19 show the resonance patterns obtained for SOS-11 at 6, 76, and 295K.

In order to further characterize the nature of the oxides, elevated temperature measurements were made to attempt to determine the magnetic transition temperatures (Néel points) of each component Superparamagnetic relaxation of hematite and magnetite occurred at temperatures lower than their respective Néel points of 956K (31) and 859K (32) At 863K, the spectrum revealed two peaks of unequal intensities and widths Figure 23 displays the resonance pattern of SOS-11 at 863K. Above the blocking temperature for superparamagnetic hematite particles, a doublet is observed (29), while superparamagnetic magnetite particles exhibit a broad singlet (33) No evidence of other magnetic phases such as calcium ferrites could be observed in any of these measurements

Based on the superparamagnetic fractions measured, some information on size of the hematite and magnetite particles can be obtained. Using data published in

McNab et al (33) and Kundig et al (29) our results show that a large percentage of the magnetic oxides exist as particles that have a diameter below 125 Å.

The transformations observed in the oxygen containing retorts pose numerous questions for relating internal conditions to the results Under strictly thermal condi tions, the carbonates siderite and ankerite have been shown to decompose to wüstite (FeO) (34) and $Ca_2Fe_2O_5$ respect ively (35) In the presence of oxygen, iron may assume a different oxidation state thus forming a variety of oxides at different oxygen fugacities Pyrite exposed to similar conditions is oxidized to hematite at elevated temperatures, via an intermediate sulfate phase (36) The presence of oxygen in the systems studied here must be a major control ling factor in the transformations observed.

Oxygen is initially introduced to each system, however it is unlikely that this persists Reactions of oxygen and carbon occur in the Paraho retort to provide heat In the modified in-situ process, oxygen most likely reacts with carbon during retorting. This means oxygen fugacity is controlled by the reactions:

$$C(s) + \tfrac{1}{2}O_2(g) \rightleftarrows CO(g)$$

$$CO(g) + \tfrac{1}{2}O_2(g) \rightleftarrows CO_2(g)$$

These reactions create a system which controls the oxygen fugacity and therefore the oxidation state of iron (34, 37)

In the Paraho and Lawrence Livermore run S-7 no significant breakdown of pyrite was observed. In runs S-10 and S-11 all of the pyrite was converted to magnetic oxides From an environmental standpoint, the question of pyrite breakdown as a function of retort conditions is indeed an important one. Pyrite oxidation has been reported to occur via two steps prior to the formation of Fe_2O_3 (38,39) Initially, pyrite is oxidized to iron sulfate ($Fe_2(SO_4)_3$) Secondly, the iron sulfate is converted to Fe_2O_3 and sulfur trioxide. The conversion of iron sulfate to hematite is very fast above 973K (39) Further study of the oxidation of pyrite via this mechanism has shown that the reaction rate is determined by the rate of diffusion of sulfur and oxygen gases (39)

In general, the diffusion of gases through a cross section of material may be related to Fick's first and second laws of diffusion (40) The diffusion of gases through solids is related to the temperature, pressure, time, and concentration of each gas in the system. The rate of diffusion of the two gases through a crystal and hence the extent of oxidation will increase by increasing any of these variables The crystal structure and particle

size of the solid will also affect the rate of oxidation.

In the systems studied here, the conditions vary significantly from one retort to another. The concentration of oxygen, time of retorting, and the temperature within the systems are the three variables that will control to some extent pyrite oxidation. Also, as the temperature of the shale rises, carbonate breakdown will create greater permeability for the diffusion of the gases

In the Paraho process and in S-7, pyrite oxidation is not noticeable; in S-10 and S-11, complete oxidation is observed. The diffusion rates of the gases in S-7 and the Paraho process must not be such as to incur pyrite oxidation during the time of retorting. In S-10 and S-11, diffusion rates coupled with other processes that increase with temperature increase the oxidation rate of pyrite such that the reaction goes to completion. This analysis of the situation suggests that in oxygen containing retorts, pyrite should oxidize. At lower temperatures, the rate of the reaction is too slow to see appreciable oxidation. This hypothesis is worthy of future experimental consideration.

In the systems studied in this paper, equilibrium has not been attained. Separate studies using x-ray diffraction have shown the presence of clays and calcite

in the spent shales. The open nature of these retorts, coupled with the relative short time the shale is maintained at those conditions, do not allow equilibration of the minerals with the gaseous environment to occur. A key factor to consider in determining mineral equilibration is the openness of the system. A study of the reactions of the minerals in oil shale in closed systems will be presented at a later date (41)

This study has indicated a trend to the formation of oxides as the retorting temperature and oxygen fugacity increase. These results are consistent with metamorphic reactions observed in dry environments (42) The presence of hematite and magnetite which have formed from carbonates and sulfides represent stable assemblages in an oxygen buffer system (34, 37, 43, 44) The oxygen fugacity within the Fe-O-Si system has been shown to control the formation of the mineralogic phases at elevated temperatures (44, 45) In the shales studied, Si is indeed present but does not react with Fe in an observable amount during retorting. Apparently, the oxygen fugacity in these retorts is significantly higher than that which will enable Fe and Si to react and maintain a stable assemblage (34, 37, 44) The iron minerals may be used to monitor the internal conditions within a retort

by comparing the Mössbauer analysis to the assemblages proposed by Eugster and Wones (44) Thus, if the oxygen levels in a retort are maintained at levels low enough to form iron containing silicates, trace elements may well be controlled as Smith and others (3) have proposed.

CONCLUSIONS

Through the Mössbauer studies on these shales, the following may be concluded:

1) The iron minerals identified within unretorted shales vary with the location of deposition. The minerals may be classified into three groups: 1) carbonates, 2) sulfides, and 3) clays. Ankerite is the major iron containing mineral throughout the samples studied. Identification of the minerals requires great care due to overlapping resonances

2) In the indirectly heated retorts, pyrite decomposes via a reaction with hydrogen to produce pyrrhotite. This decomposition occurs at temperatures far below the ones expected for pyrite segregated from hydrogen. The carbonates remain unchanged.

3) Within the retorts containing oxygen, the minerals hematite and magnetite are observed as the decomposition products of the original minerals The presence of these two minerals implies that a static buffer system may be present within each retort. If this is the case, the oxygen fugacity may be estimated on the basis of temperature and the presence of the two oxides.

4) In the retorts containing oxygen, pyrite appears to be stable up to 1023K.

5) Based on conclusions 2, 3, and 4, the iron minerals may be used to follow the internal conditions that exist within a given retort by following their transformations

6) The control of certain trace elements which are thought to reside in pyrite may be attempted by controlling retort conditions such that pyrite breakdown does not occur

REFERENCES CITED

1 Fox, J.P., McLaughlin, R.D., Thomas, J.F., and Poulson, R.E. Proceedings Tenth Oil Shale Symposium 1977, Colorado School of Mines Press, 223.

2. Kilburn, P.D., Atwood, M.T , and Broman, W.M. Guidebook of the Energy Resources of the Piceance Creek Basin, Colorado (Ed. D.K. Murray), Rocky Mountain Assn. of Geologists 1974, p. 151

3. Smith, J.W., Robb, W.A., and Young, N.B. Proceedings Eleventh Oil Shale Symposium 1978, Colorado School of Mines Press, 100.

4. Wildeman, T.R. and Meglen, R.R. Analytical Chemistry of Oil Shale and Tar Sands, Advances in Chemistry Series, No. 170, 195.

5. Saether, O.M., Runnels, D.D., and Meglen, R.R. Trace Elements in Oil Shale, Progress report contract No. EV-10298 Department of Energy, 236.

6. Brobst, D.A. and Tucker, J.D. United States Geological Survey Professional Paper 803, 53 p., 1973.

7 Desborough, G.A. and Pitman, J.K. Guidebook to the Energy Resources of the Piceance Creek Basin, Colorado (Ed. D.K. Murray) Rocky Mountain Assn. of Geologists 1974, 81

8. Cole, R.D., Liu, J-H., Smith, G., Hinckley, C.C and Mykola, S. Fuel 1978, 57, 514

9. Campbell, J.H. and Burnham, A.K. Proceedings Eleventh Oil Shale Symposium 1978, Colorado School of Mines Press, 242.

10. Jukkola, E.E., Denilauler, A.J., Jensen, H.B., Barnet, W.I , and Murphy, W.I.R. Industrial and Engineering Chemistry 1953, 45, 2711

11 Arnold, R.G. Economic Geology 1962, 57, 72

12. Wildeman, T.R. A Summary of Oil Shale Activities at the National Bureau of Standards 1975-1979 (Ed. L.T McClendon) EPA-IAG-D5-E684

13. Wildeman, T.R. and Heistand, R.N. Preprints Div. Fuel Chem., ACS 1979, 24, 271

14 Wildeman, T.R. Preprints Div. Fuel Chem., ACS 1977, 22(2), 760.

15 Jones, J.B. Jr. Quarterly of the Colorado School of Mines 1976, 71(4), 39.

16 Rothman, A.J Quarterly of the Colorado School of Mines 1975, 70(3), 159.

17 Goodfellow, L. and Atwood, M.T Quarterly of the Colorado School of Mines 1974, 69(2), 205.

18. Forester, D.W. and Koon, N.C. Journal of Applied Physics 1969, 40(3), 1316.

19. Smith, J.W. and Robb, W.A. Journal of Sedimentary Petrology 1966, 36, 486.

20. Lefelhocz, J.F., Friedel, R.A. and Kohman, T.P Geochimica et Cosmochimica Acta 1967, 31, 2261

21 Morice, J.A., Rees, V.C. and Rikard, D.T Journal of Inorganic and Nuclear Chemistry 1969, 31, 3797

22 Montano, P. Preprints Division Fuel Chemistry, ACS 1979, 24(1), 218.

23. Huffman, G.P. and Huggins, F.E. Fuel 1978, 57, 592

24 Maxwell, E., Jacobs, I.S., Kelland, D.R. and Levinson, L.M. General Electric Technical Information Series 1980, 80CRD162, p. 18.

25. Craig, J.R. and Scott, S.D. Sulfide Mineralogy, Mineralogical Society of America 1974, Short Course notes, 1

26. Robinson, L. Hydrocarbon Processing 1978, 11, 213.

27 Montano, P., Preprints Div. Fuel Chem., ACS 1980.

28. Novikov, G.V., Al'Iber, S.E., Rubtsov, V.A., Sokolov, Y.A. and Yegorov, N.K Geochemistry International 1976, 1, 86.

29. Kündig, W., Bömmel, H., Constabaris, G. and Lindquist, R.H. Physical Review 1968, 167(2), 533.

30. Mada, J. and Iida, S. Journal of the Physics Society of Japan 1975, 39(6), 1627

31 Van der Woude, F Physics Status Solidi 1966, 17, 417

32. Van der Woude, F., Sawatzky, G.A. and Morrish, A.H. Physical Review 1968, 167(2), 533.

33. McNab, T K , Fox, R.A. and Boyle, A.J F Journal of Applied Physics 1968, 39(2), 5703.

34. French, B. American Journal of Science 1971, 271, 37

35. Dasgupta, D.R. Mineralogical Magazine 1965, 35(272), 634

36. Schwab, G., Schwab, M. and Philinis, J Journal of the American Chemical Society 1947, 69, 2558.

37 Eugster, H.P. and Skippen, G.B. Researches in Geochemistry (ED. P.H. Abelson), John Wiley and Sons 1968, 492

38. Marusak, L.A., Walker Jr , P.L. and Mulay, L.N. IEEE Transactions on Magnetics 1976, Mag-12(6), 889.

39. Marusak, L.A. and Mulay, L.N. Journal of Applied Physics 1979, 50(11), 7807

40. Moore, W.J Physical Chemistry 4th Ed., Prentice Hall 1972, 977 p.

41 Melchior, D.C In preparation.

42. Winkler, H.G.F Petrogenesis of Metamorphic Rocks 4th Ed , Springer-Verlag 1976, 334 p.

43. Eugster, H.P. Researches in Geochemistry (Ed. P.H. Abelson), John Wiley and Sons Inc. 1959, 397

44 Eugster, H.P. and Wones, D.R. Journal of Petrology 1962, 3, 82

45. Yui, S. Economic Geology, 61, 768.

46. Bancroft, G.M. Mössbauer Spectroscopy, An Introduction for inorganic chemists and geochemists, John Wiley and Sons 1973, 252 p.

47 Stevens and Stevens, Mössbauer Effect Data Index 1970, Plenum Press

48. Williamson, D.L., Guettinger, T. and Dickerhoof, D.W. "Recent Chemical Applications of Mössbauer Spectroscopy", in Advances in Chemistry Series, (Ed. J.G. Stevens and G.K. Shenoy), ACS, Washington, In Press

49. Morice, J.A., Rees, V.C. and Rikard, D.T Journal of Inorganic and Nuclear Chemistry 1969, 31, 3797

50 Lefelhocz, J.F., Friedal, R.A. and Kohman, T P. Geochimica et Cosmochimica Acta 1967, 31, 2261

51 Daniels, J.M. and Rosencwaig, A. Journal of Physics and Chemistry of Solids 1969, 30, 1561

APPENDIX A FIGURES

The following symbols have been used in the subsequent pages to denote the resonance attributed to the minerals present.

Po	Pyrrhotite
Py	Pyrite
Ank	Ankerite
Sid	Siderite
Ill	Illite
Hem	Hematite
Mag	Magnetite
Tr	Troilite
Super Hem + Mag	Superparamagnetic Hematite & Magnetite

FIGURE 1

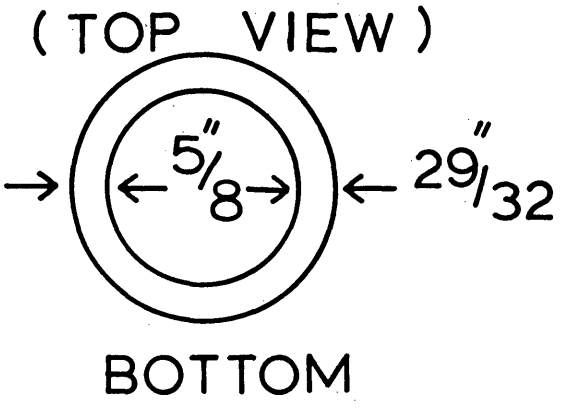

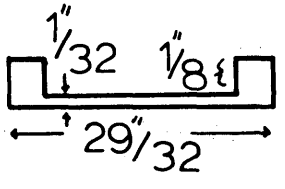

BOTTOM
(SIDE VIEW)

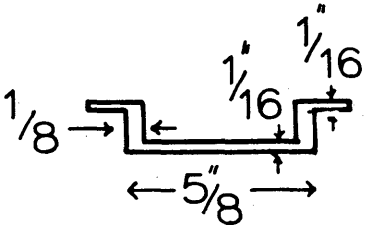

CAP
(SIDE VIEW)

GRAPHITE VESSEL

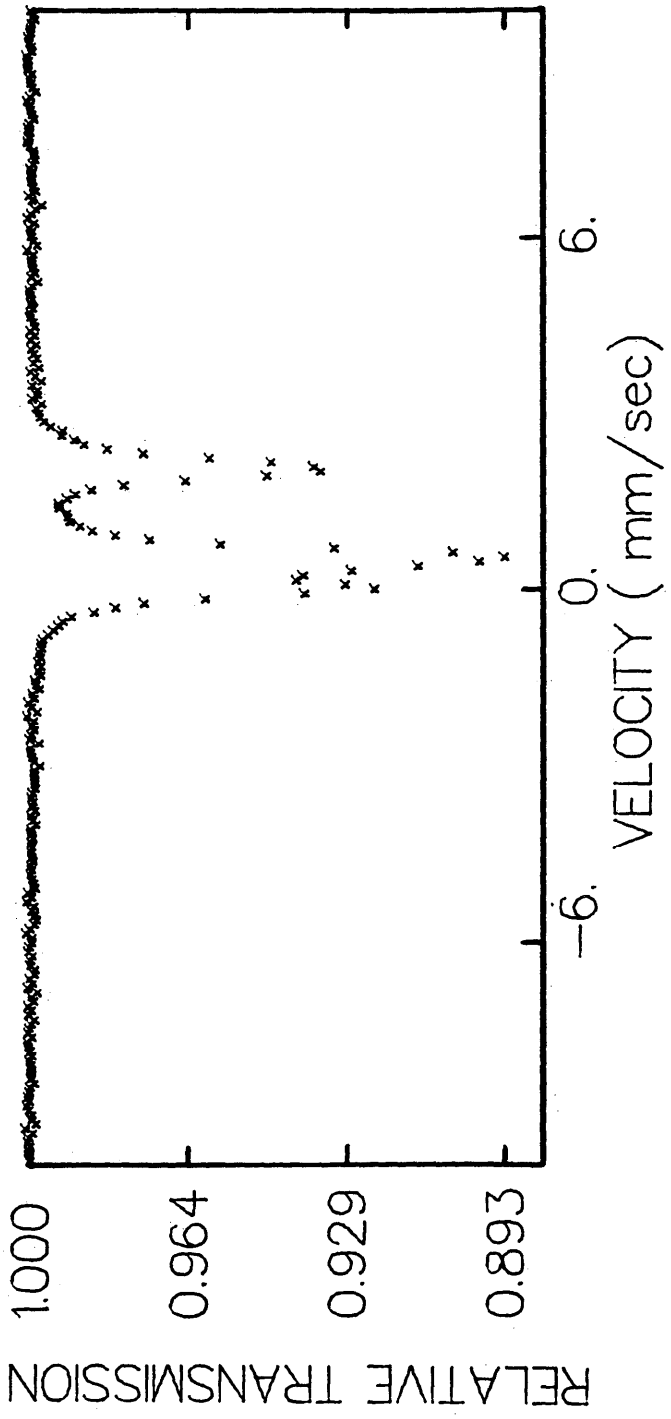

Figure 2. TOSCO unretorted shale OS-1 Spectrum 457 run at 295K.

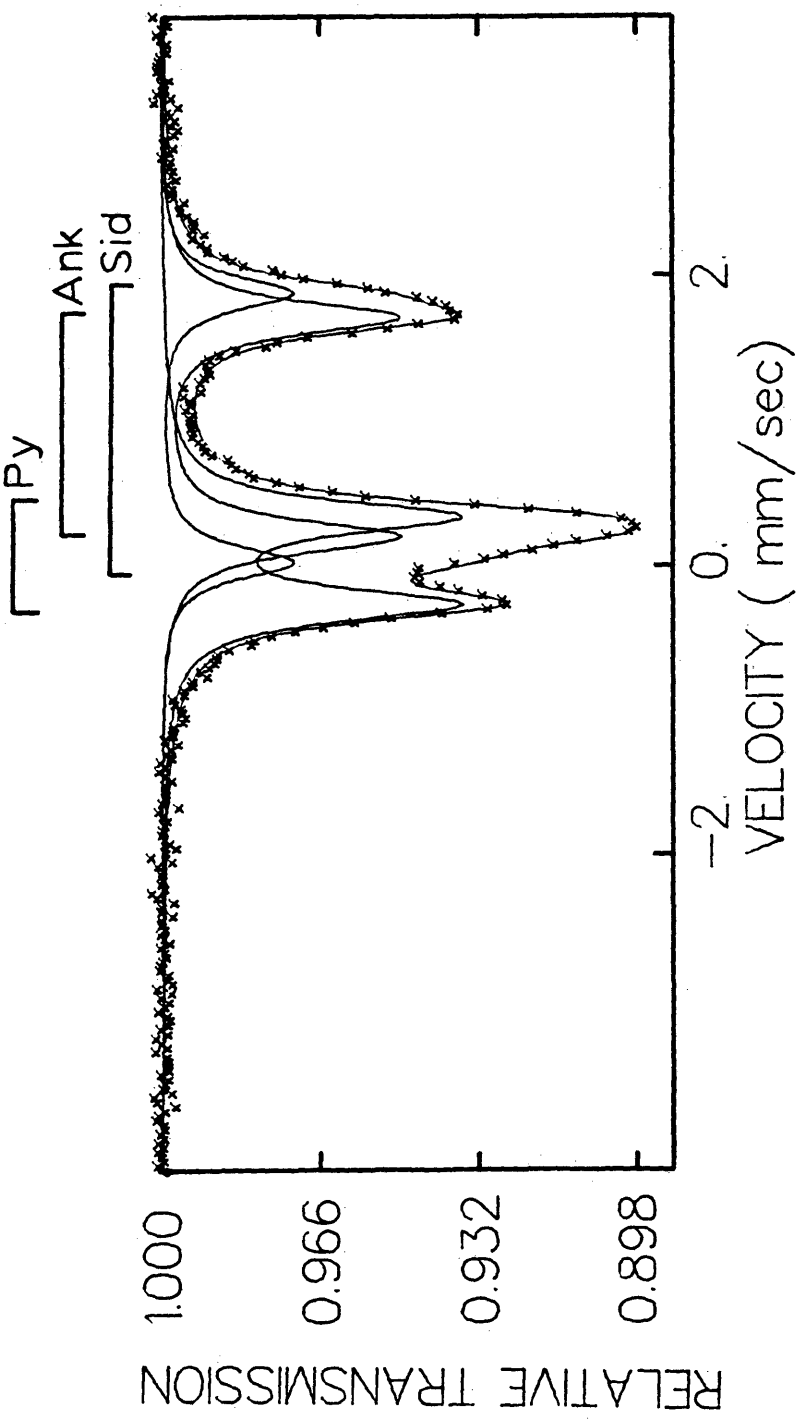

Figure 3. TOSCO unretorted shale OS-1. Spectrum 549 run at 301K.

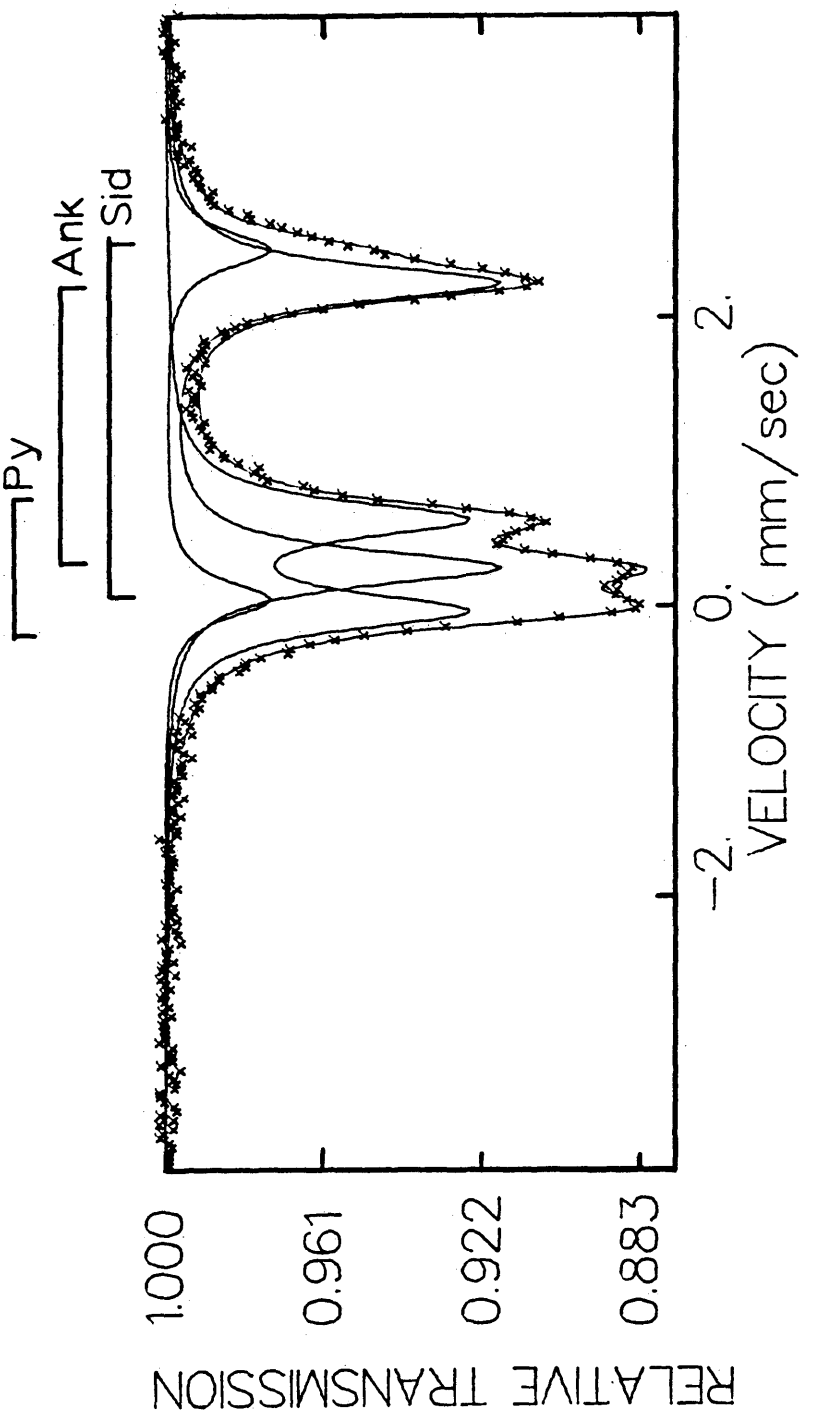

Figure 4. TOSCO unretorted shale OS-1. Spectrum 548 run at 76K.

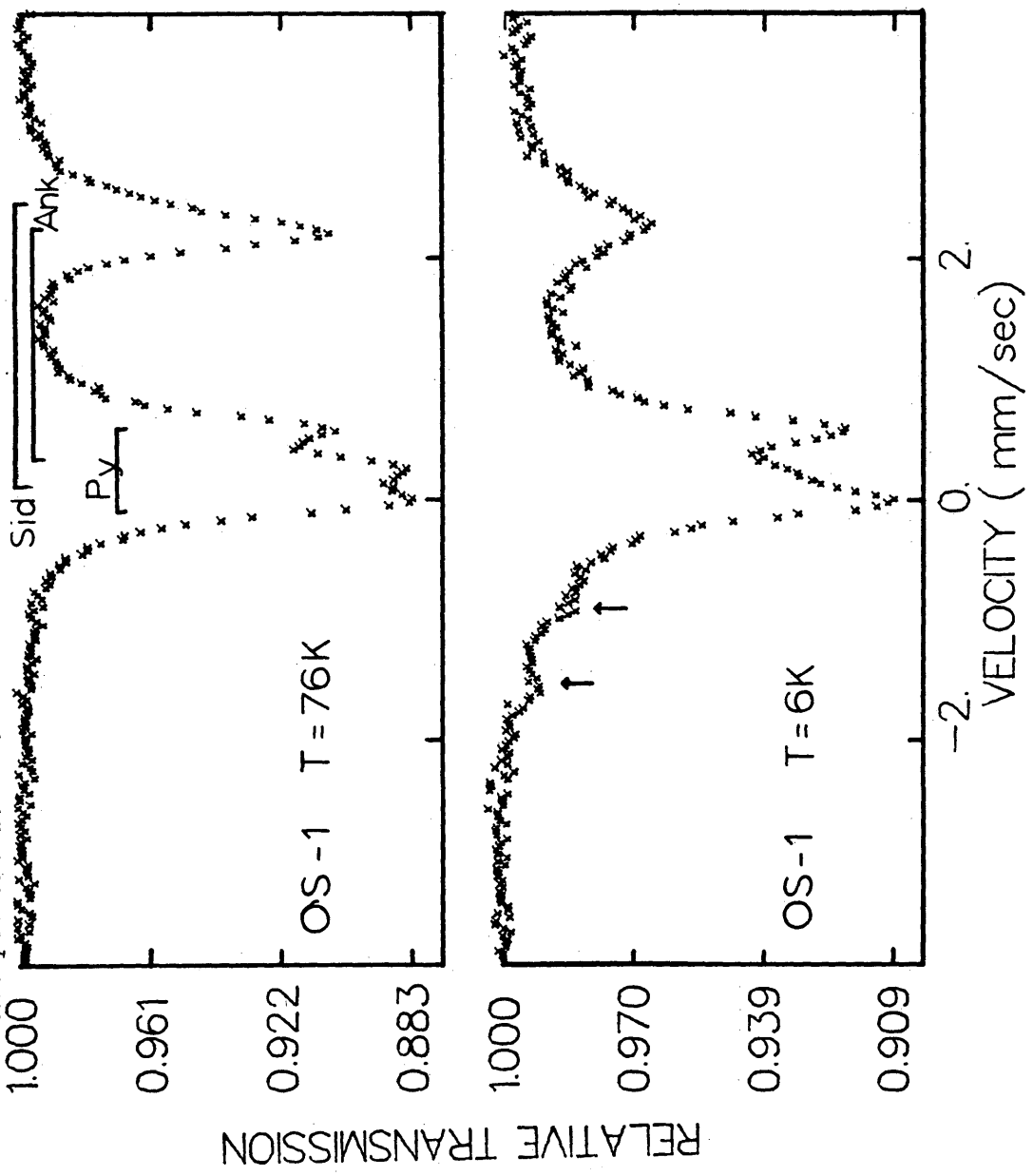

Figure 5. TOSCO unretorted shale OS-1. Spectrum 577 at 6K, spectrum 548 at 76K. Arrows present on 577 display magnetic resonance observed at 6K while not present at 76K.

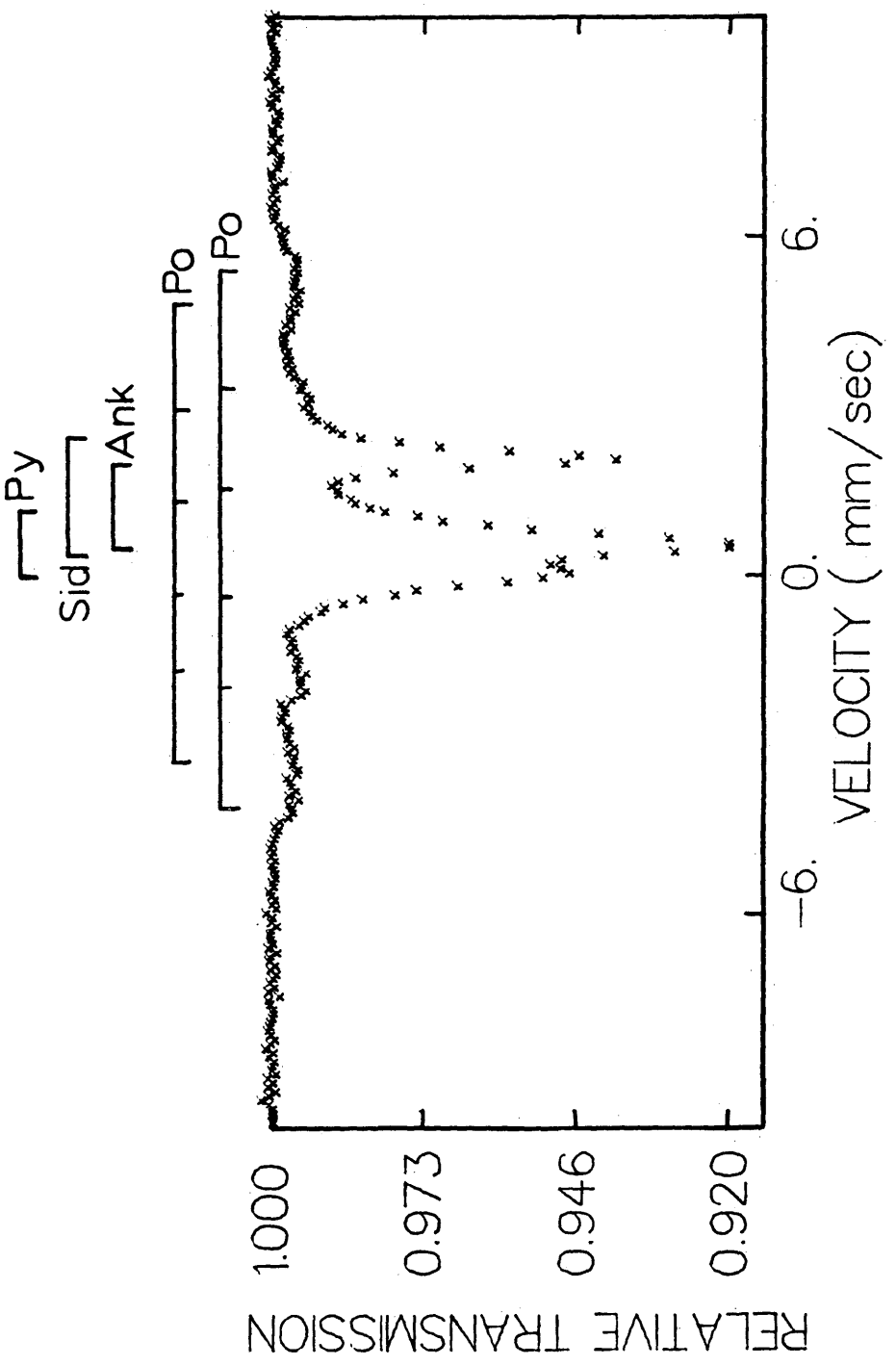

Figure 6. TOSCO retorted shale SS-2. Spectrum 456 run at 295K.

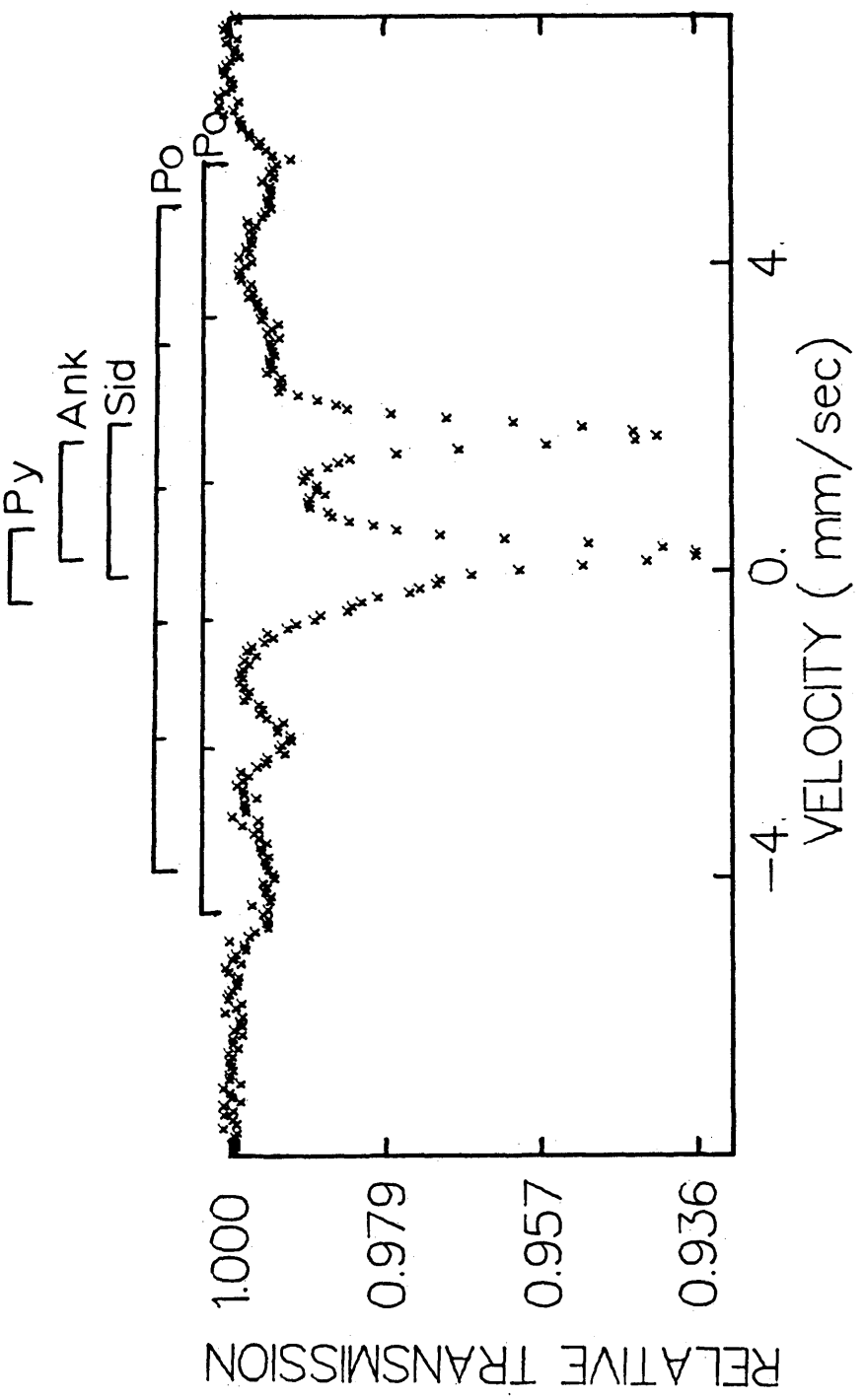

Figure 7. Fisher assay retorted shale. Spectrum 550 run at 302K.

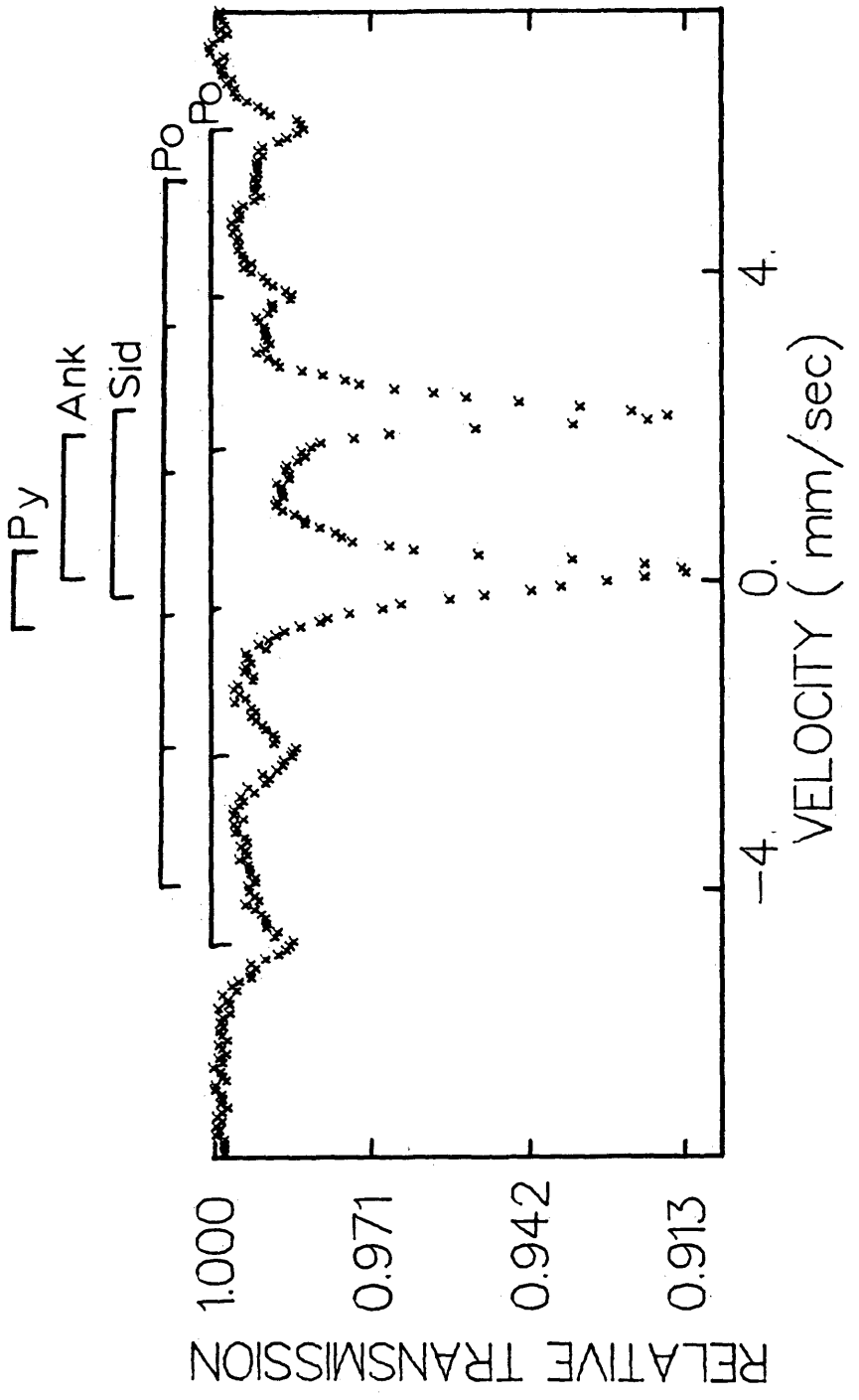

Figure 8. Fisher assay retorted shale. Spectrum 552 run at 76K.

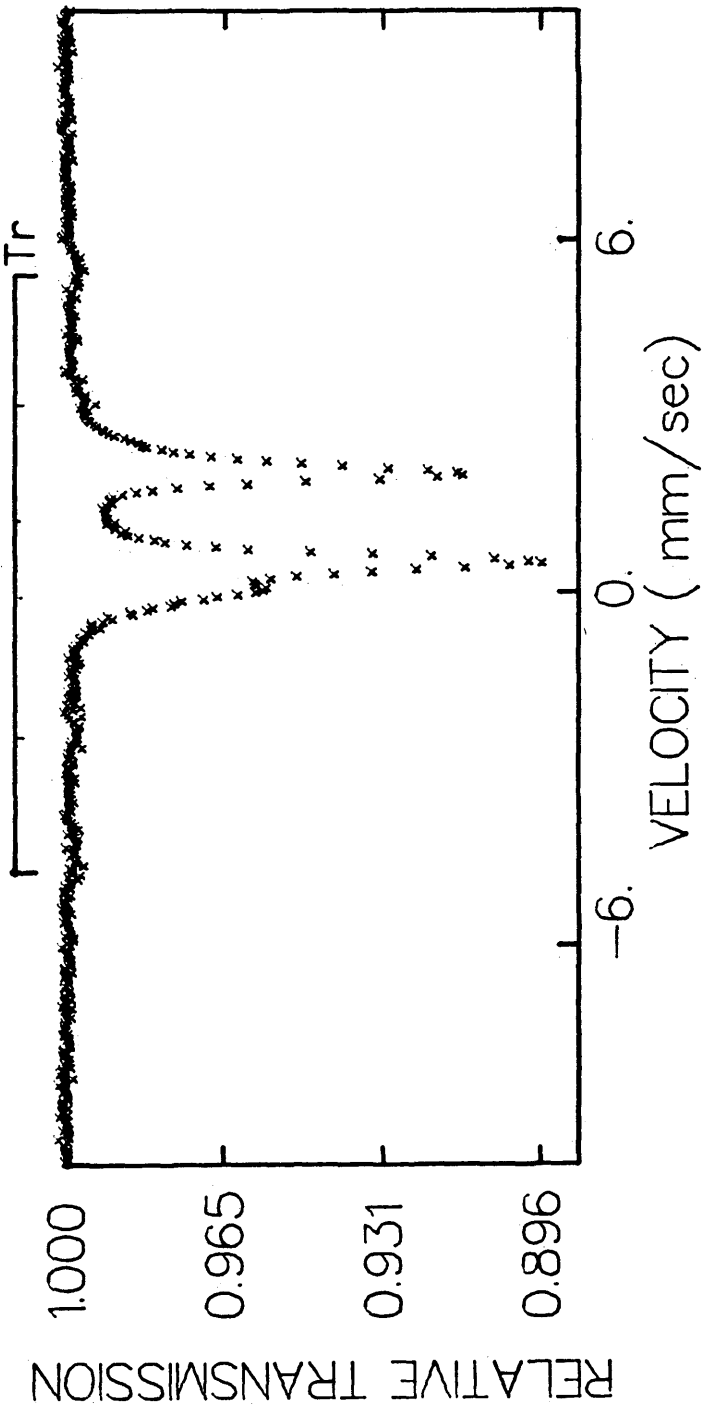

Figure 9. LLL unretorted shale Raw 1B. Spectrum 269 run at 295K.

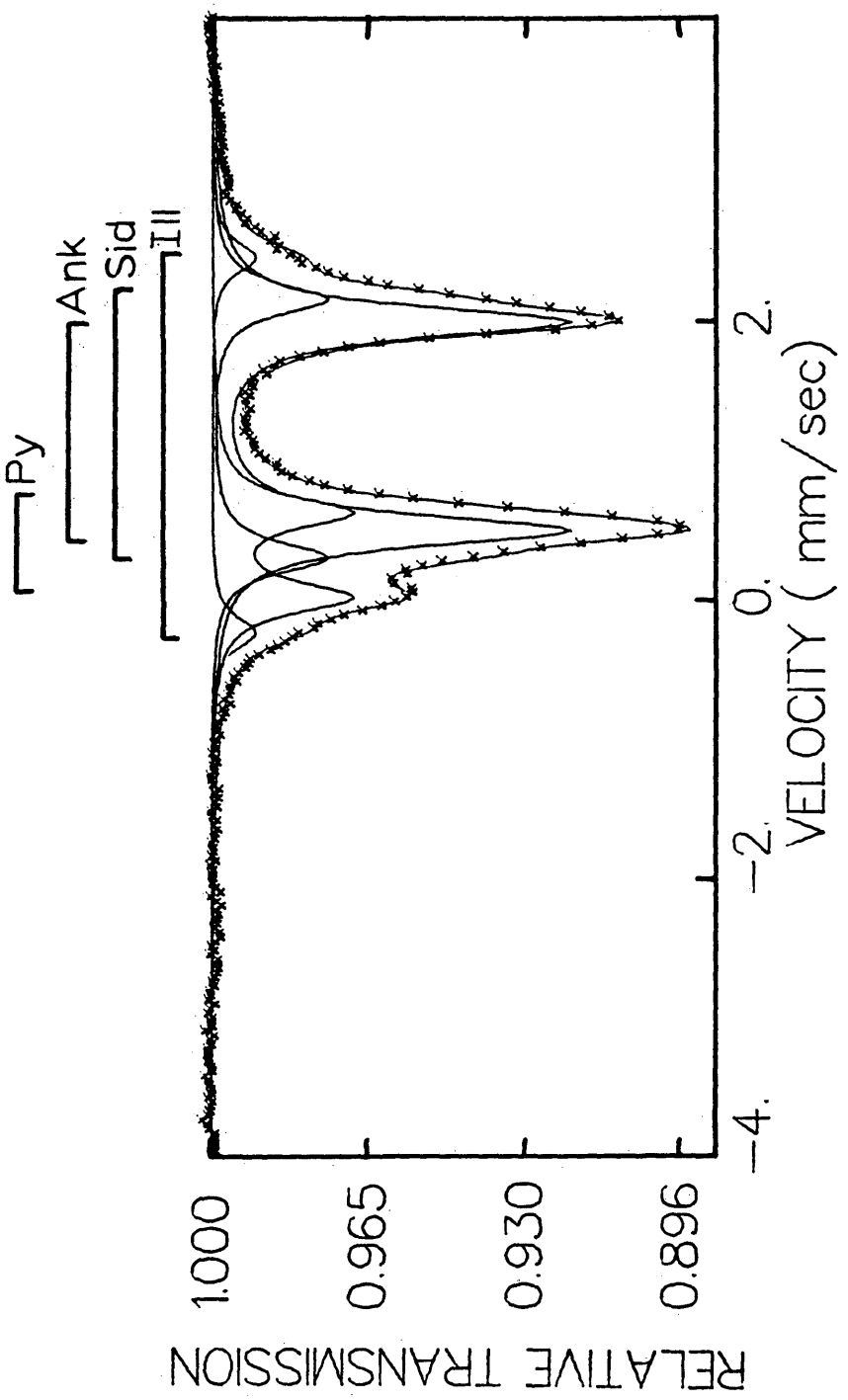

Figure 10. LLL unretorted shale Raw 1B. Spectrum 603 run at 298.5K.

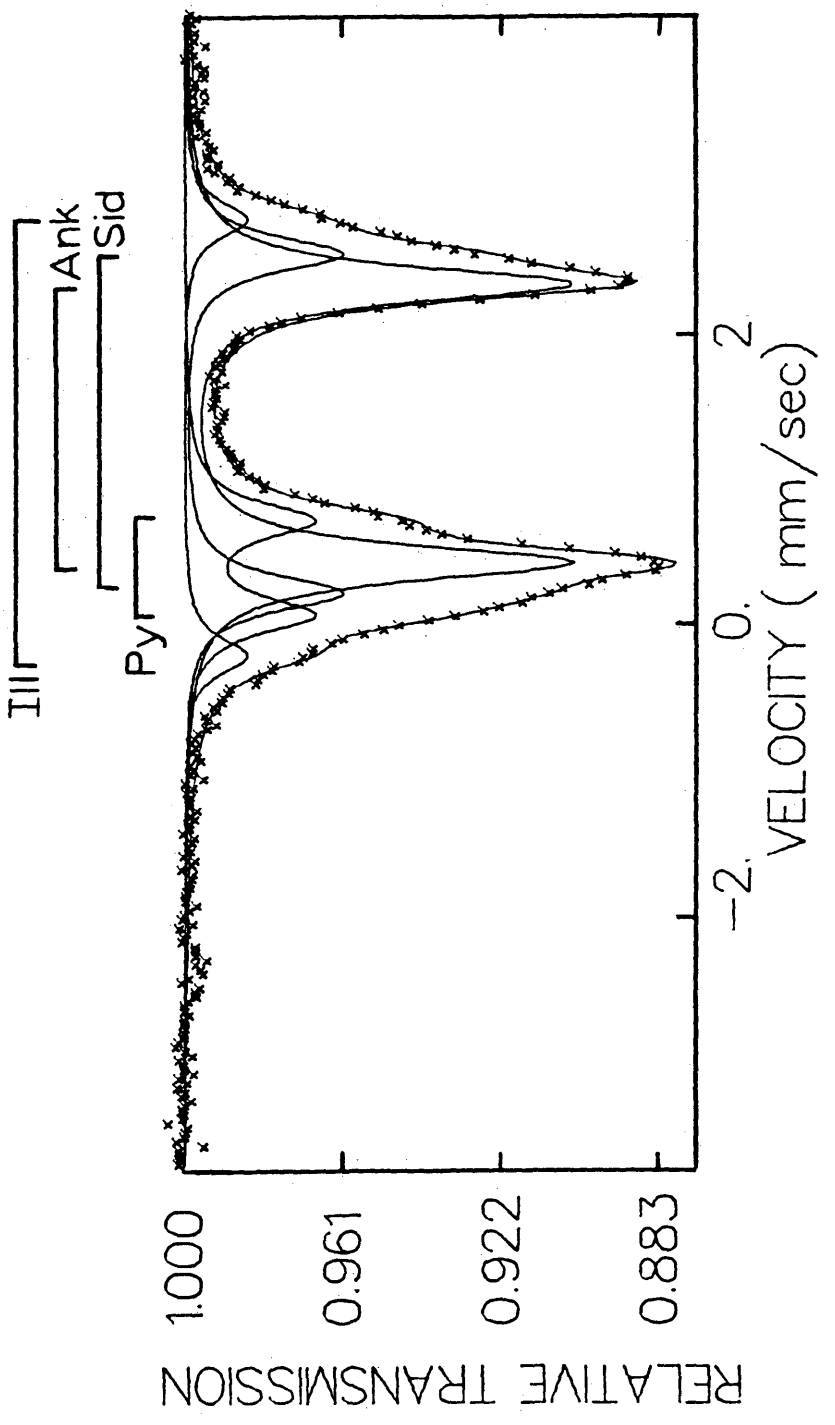

Figure 11. LLL unretorted shale Raw 1B. Spectrum 588 run at 76K.

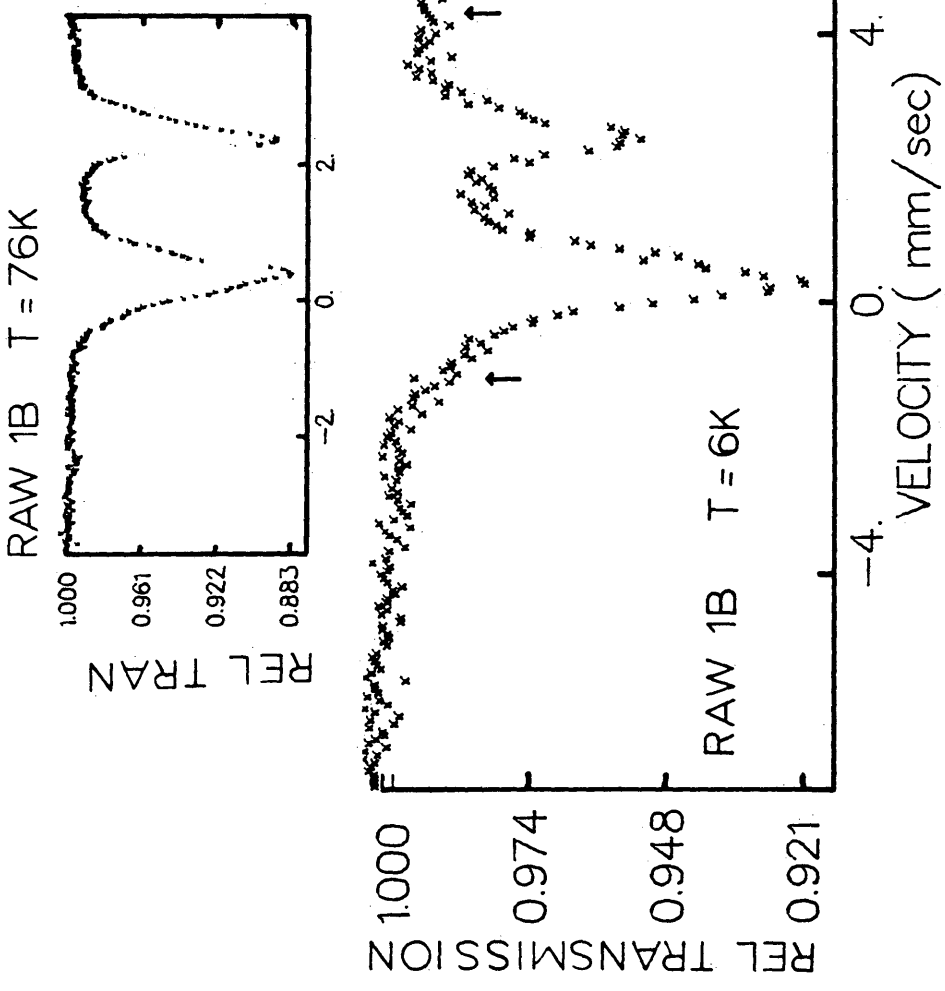

Figure 12. LLL unretorted shale Raw 1B. Spectrum 615 run at 6K, spectrum 588 run at 76K. Arrows indicate magnetic resonance observed at 6K while not present at 76K.

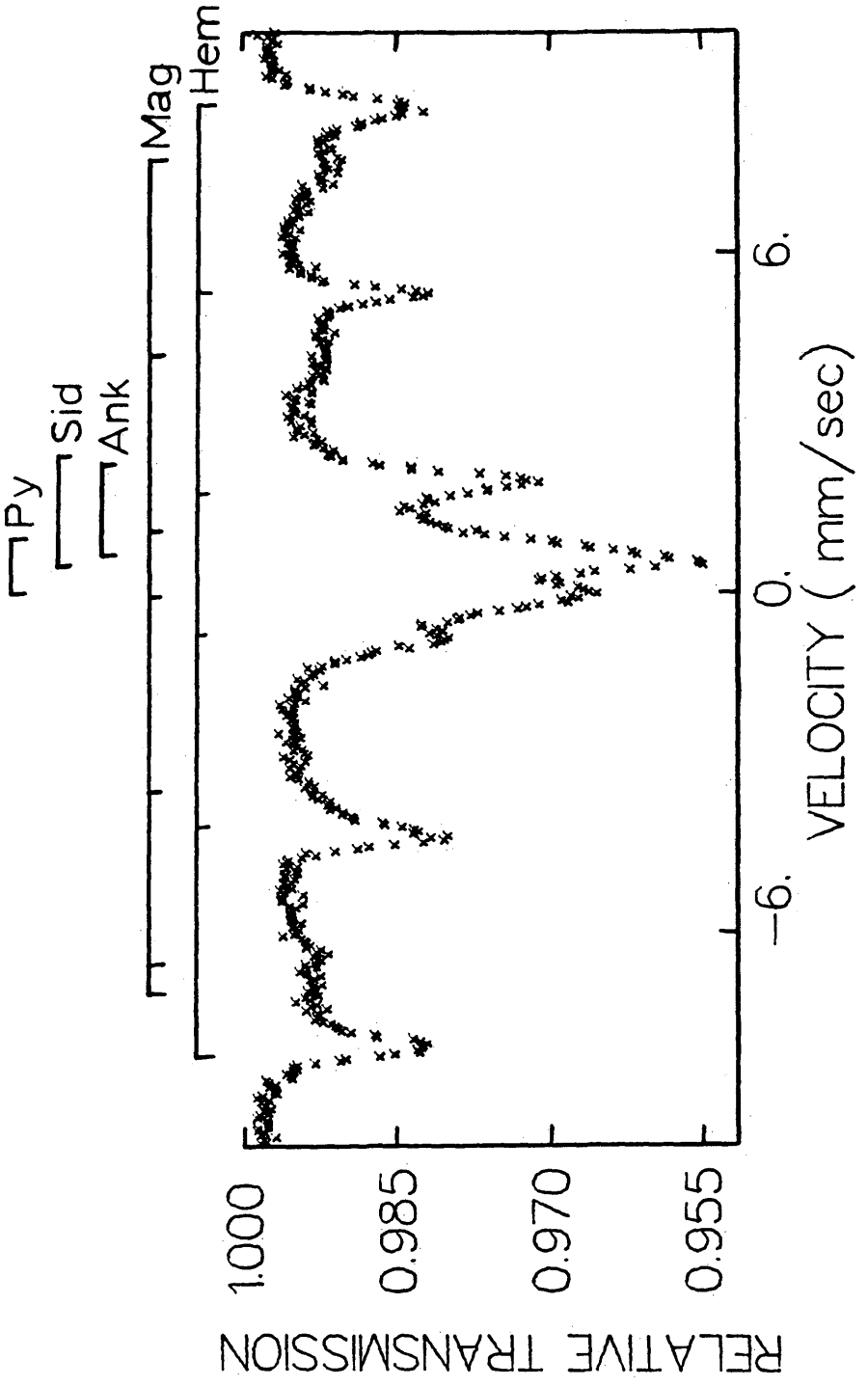

Figure 13. LLL retorted shale SOS 7. Spectrum run at 295K.

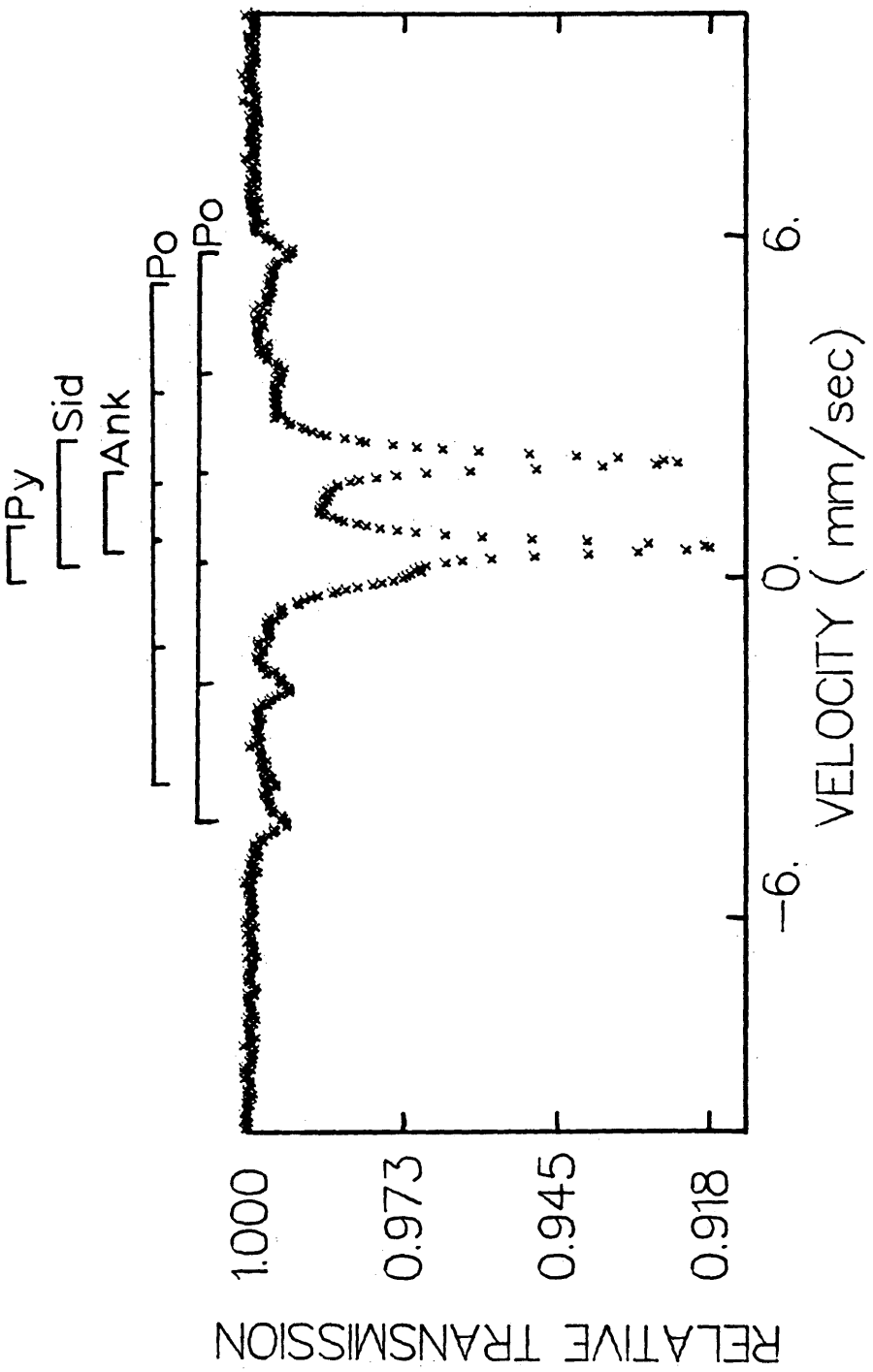

Figure 14. LLL retorted shale SOS 9. Spectrum run at 295K.

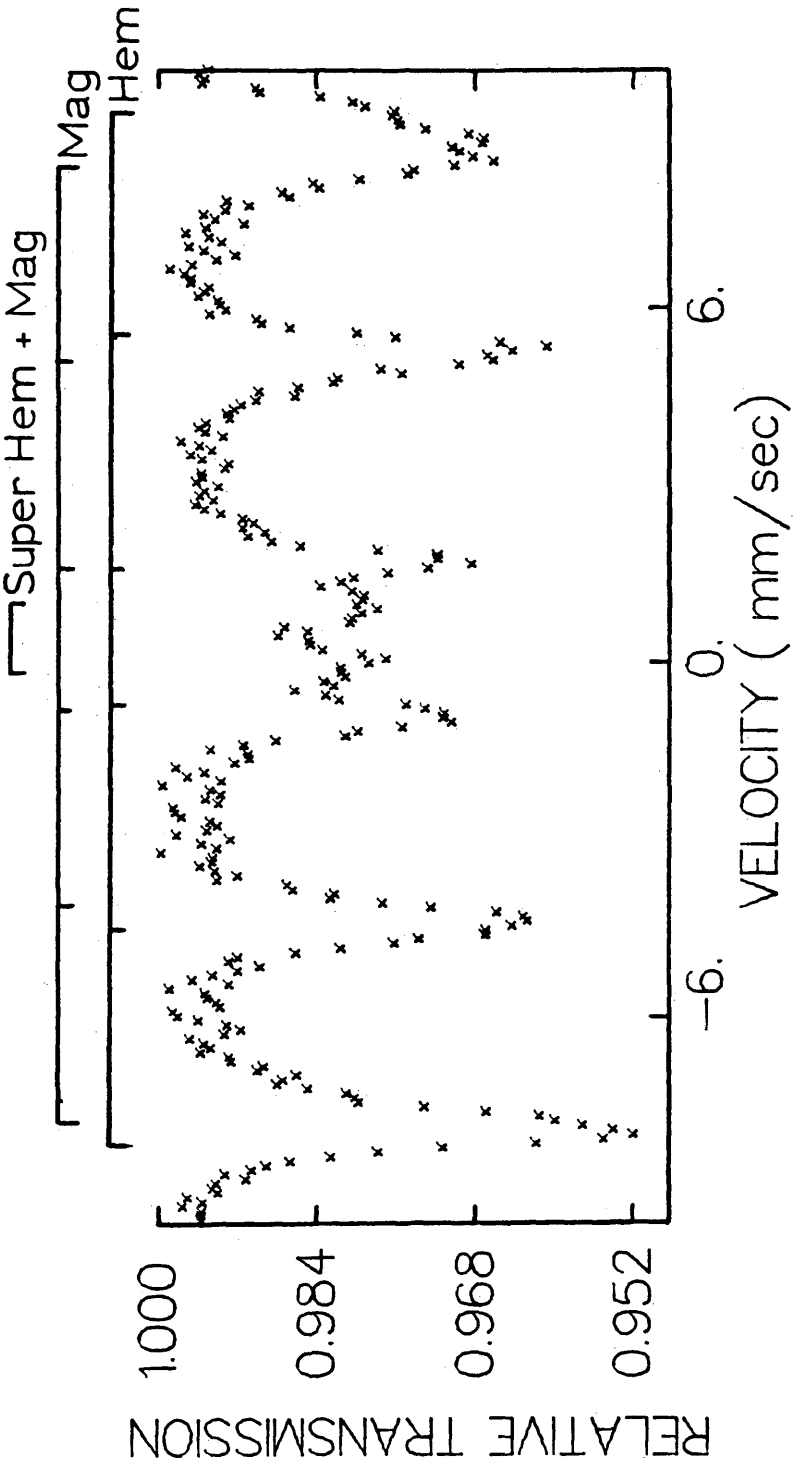

Figure 15. LLL retorted shale SOS 10. Spectrum 378 run at 76K.

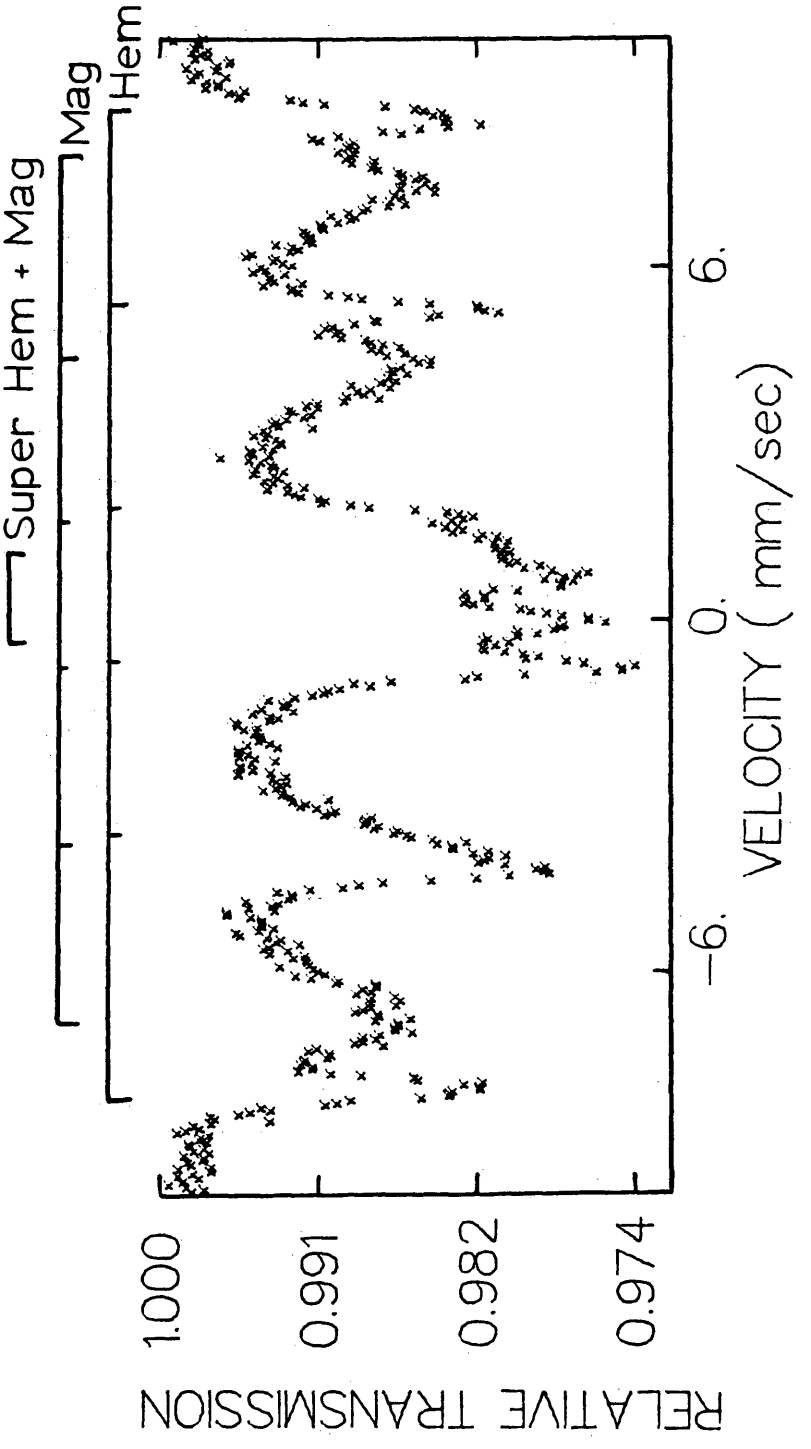

Figure 16. LLL retorted shale SOS 10. Spectrum 272 run at 295K.

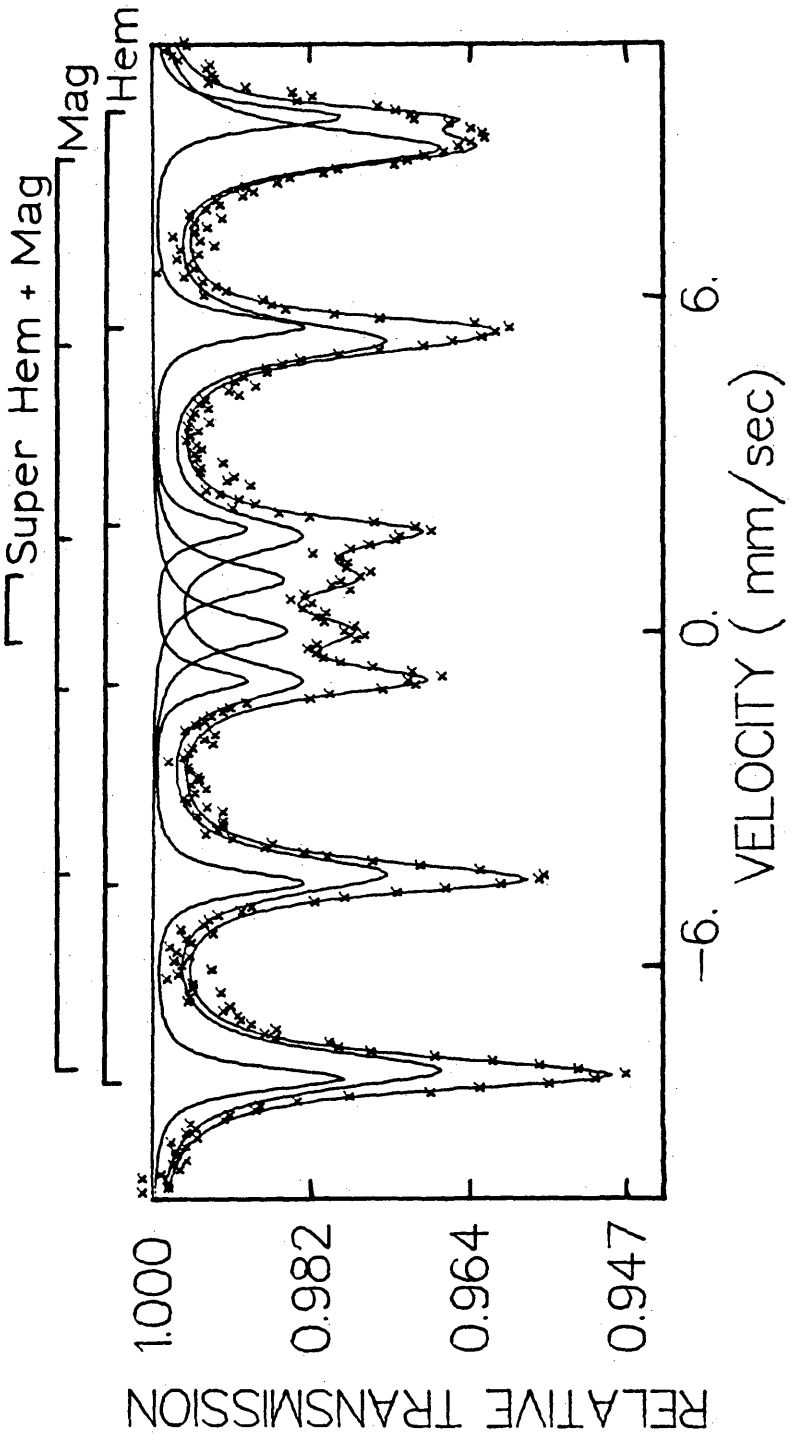

Figure 17. LLL retorted shale SOS 11B. Spectrum 575 run at 6K.

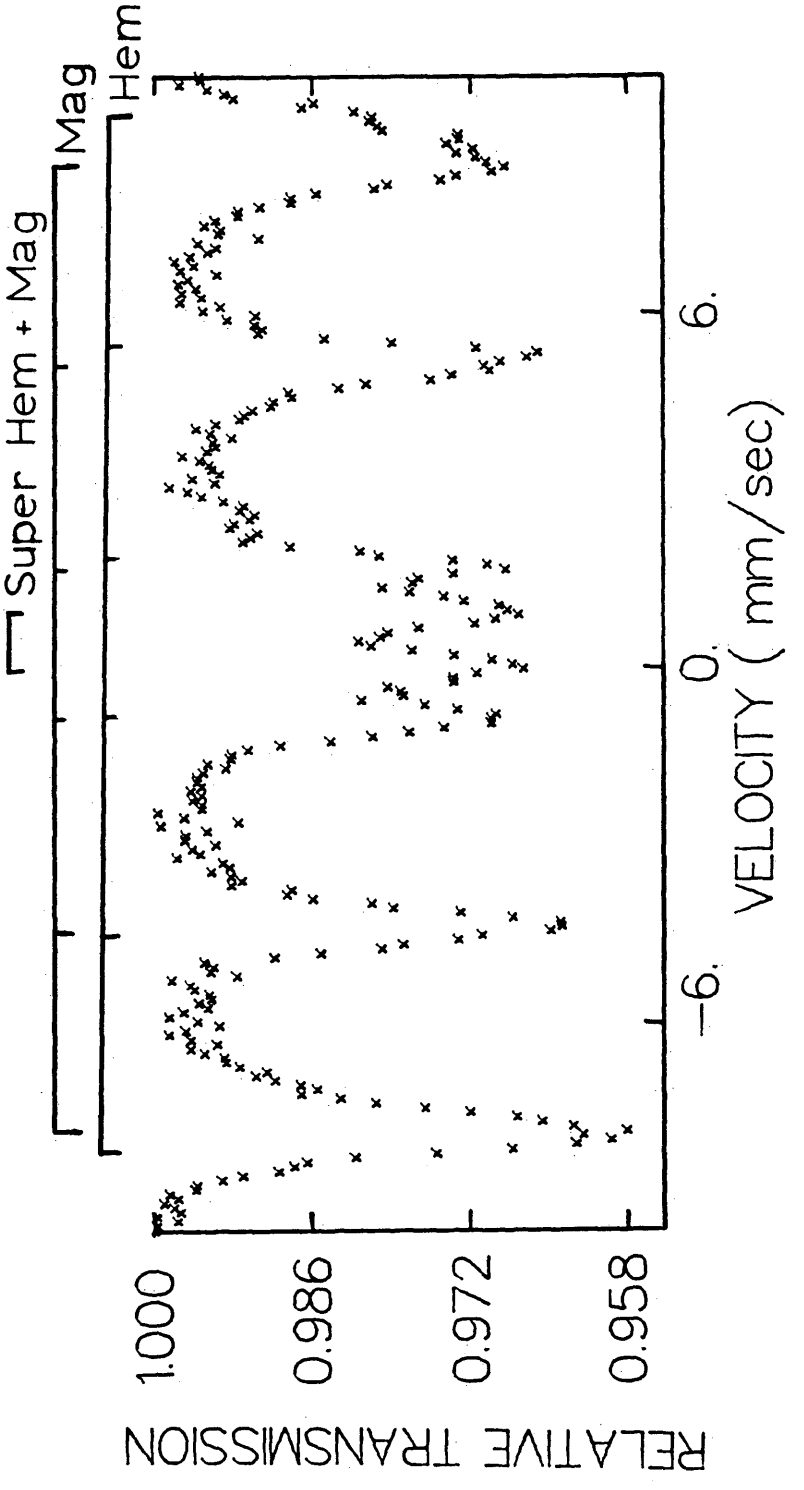

Figure 18. LLL retorted shale SOS 11B. Spectrum 377 run at 76K.

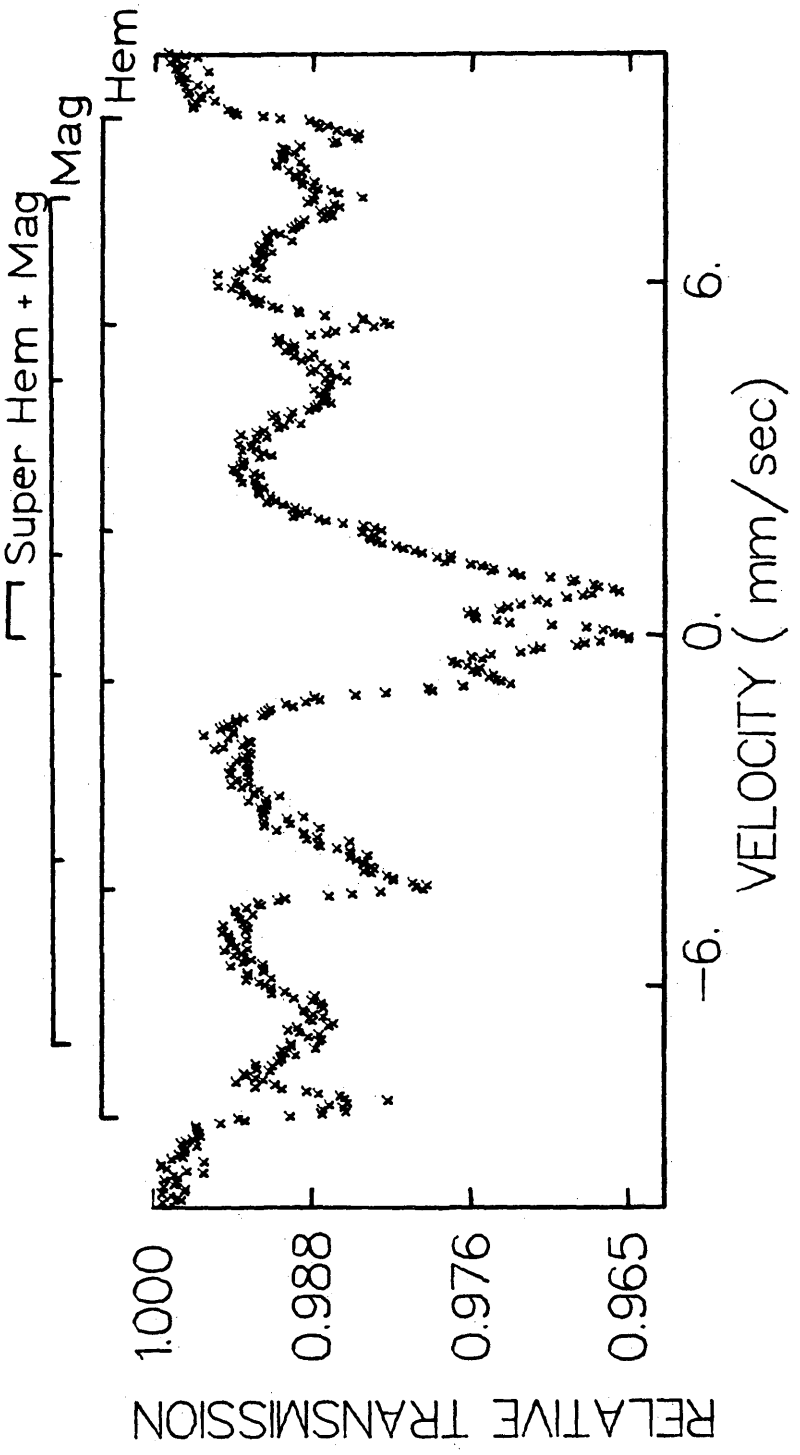

Figure 19. LLL retorted shale SOS 11B. Spectrum 266 run at 295K.

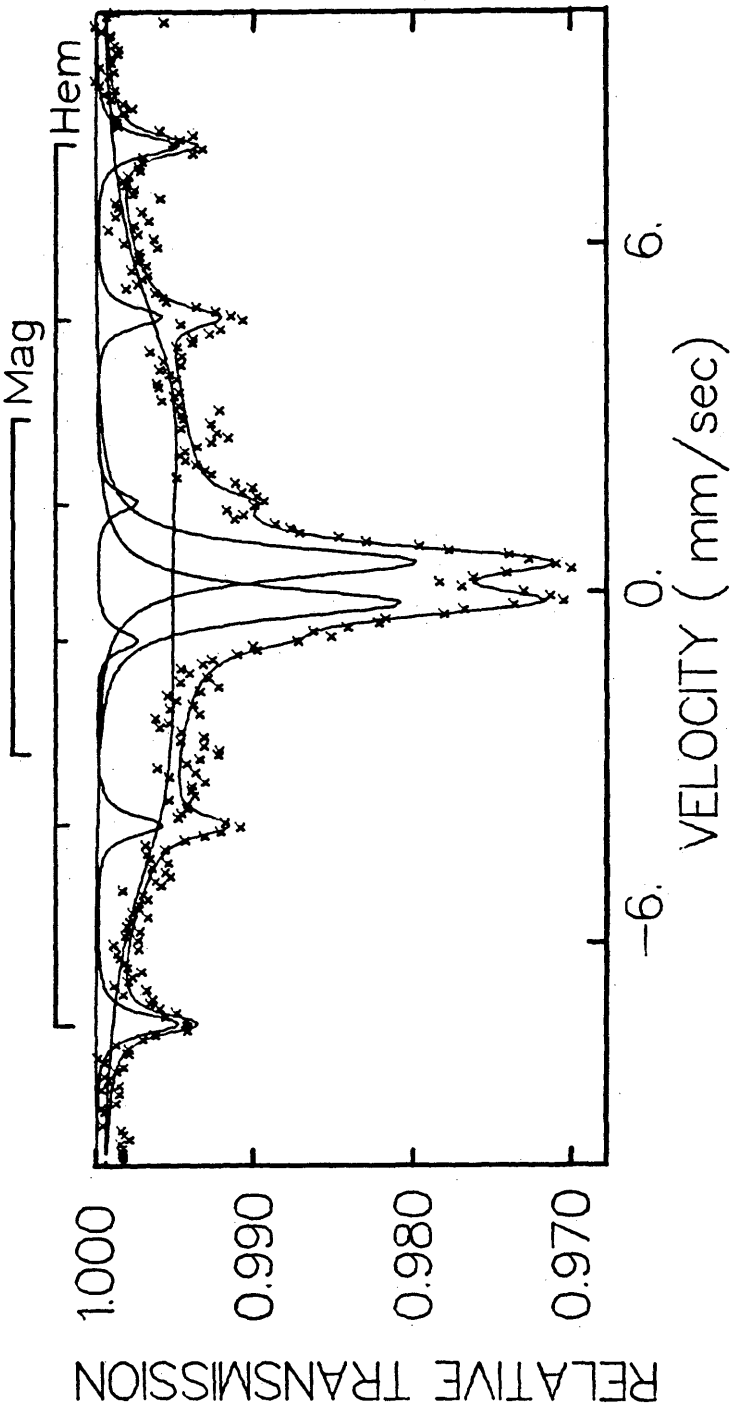

Figure 20. LLL retorted shale SOS 11B. Spectrum 556 run at 491K.

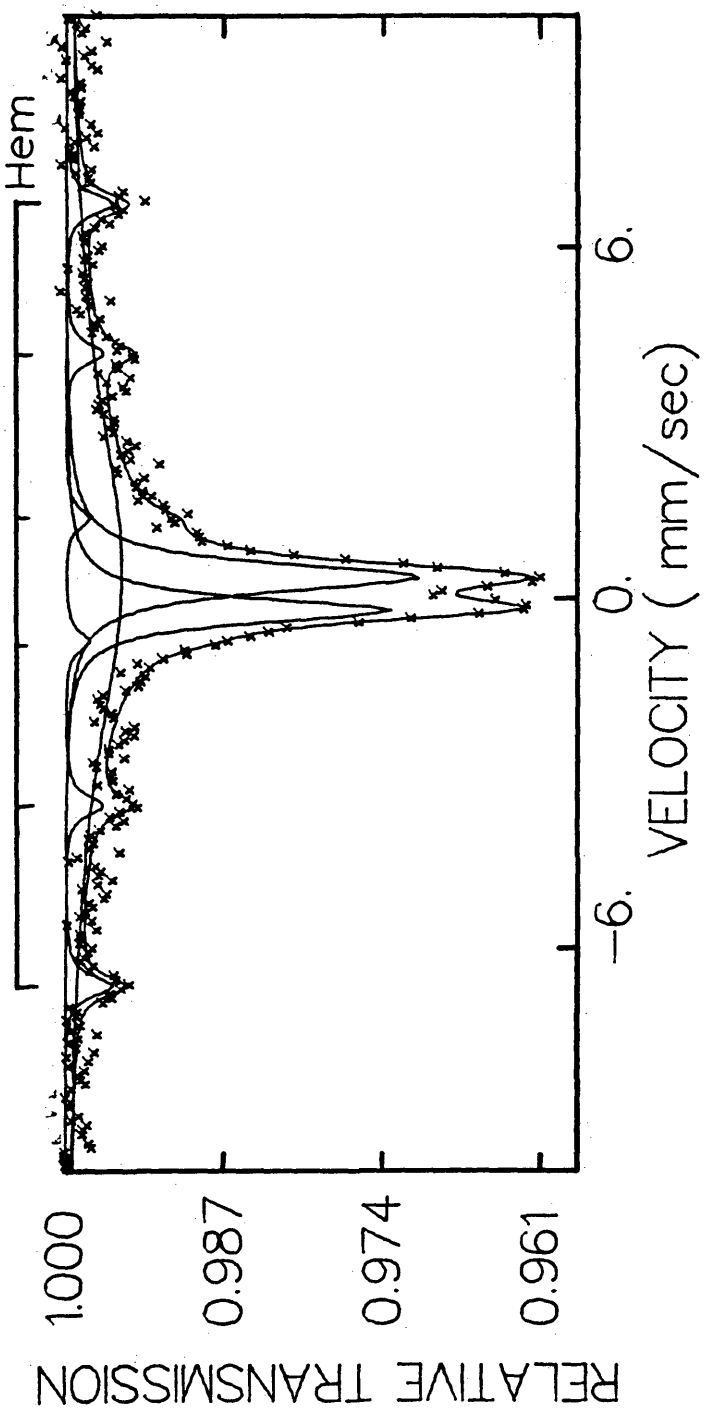

Figure 21. LLL retorted shale SOS 11B. Spectrum 557 run at 637K.

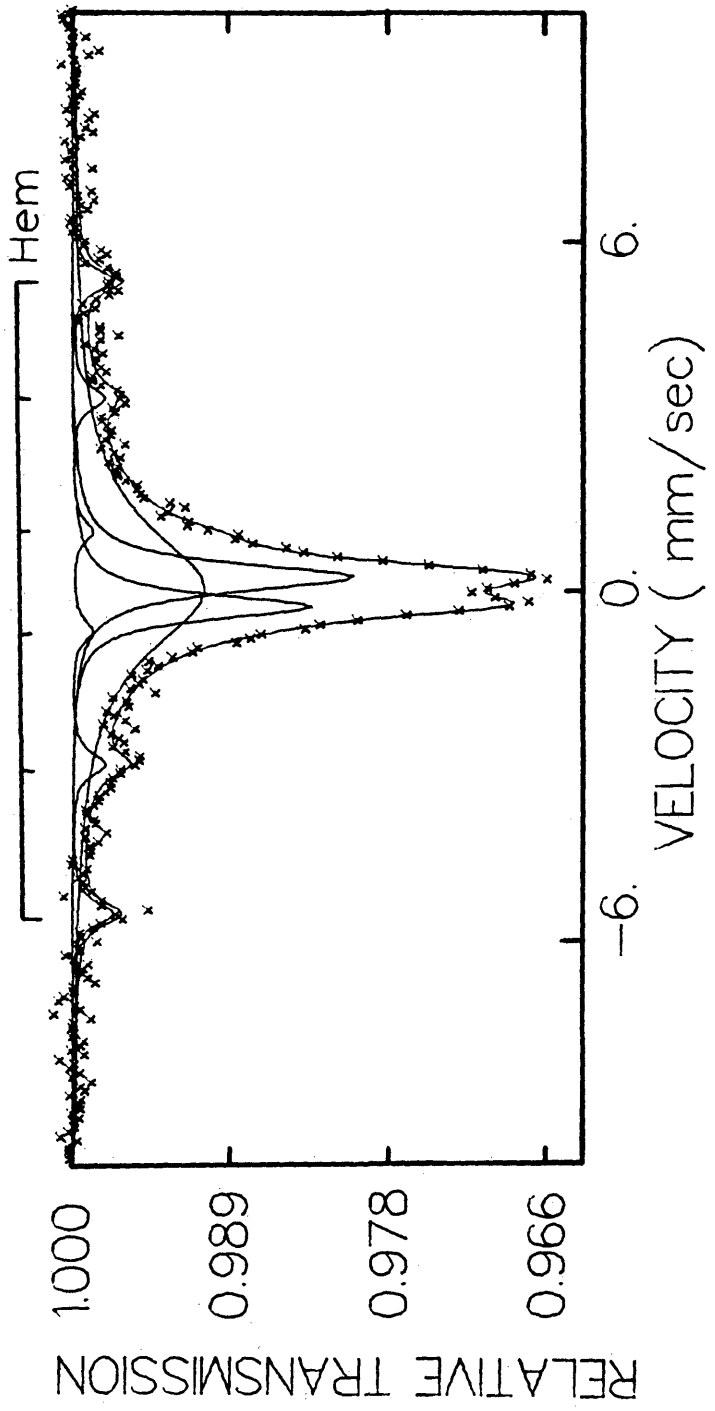

Figure 22. LLL retorted shale SOS 11B. Spectrum 558 run at 773K.

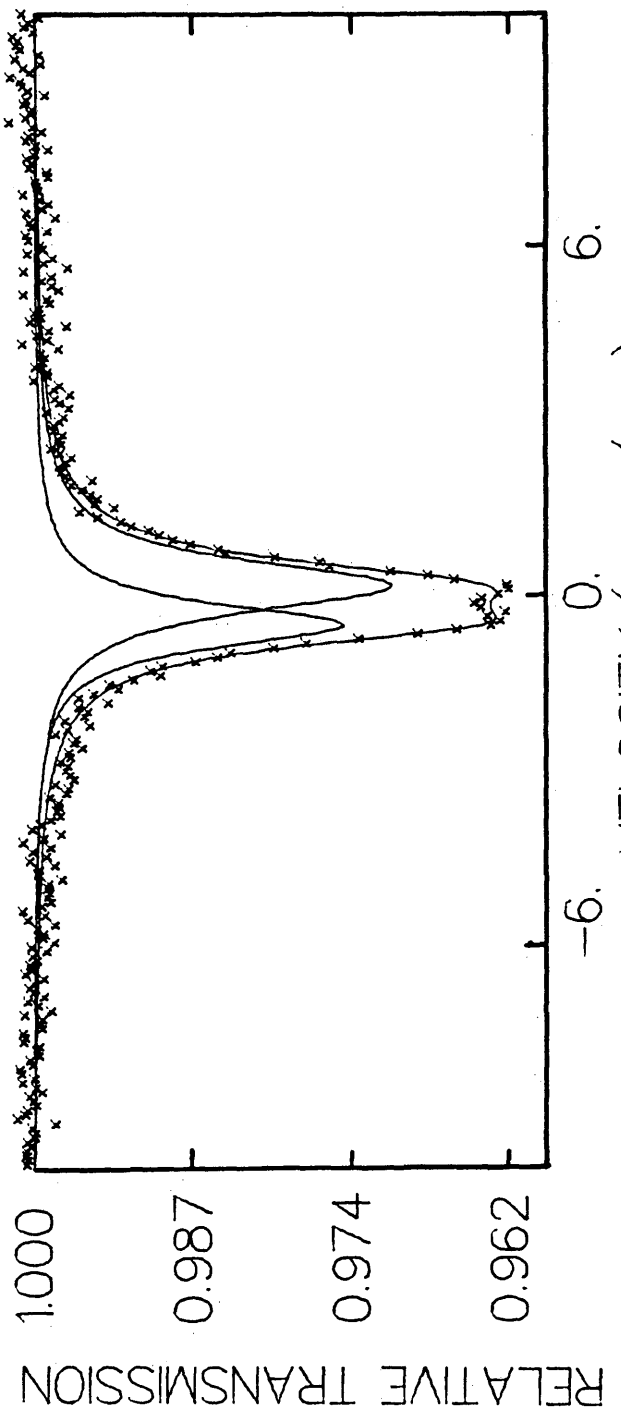

Figure 23. LLL retorted shale SOS 11B. Spectrum 559 run at 863K.

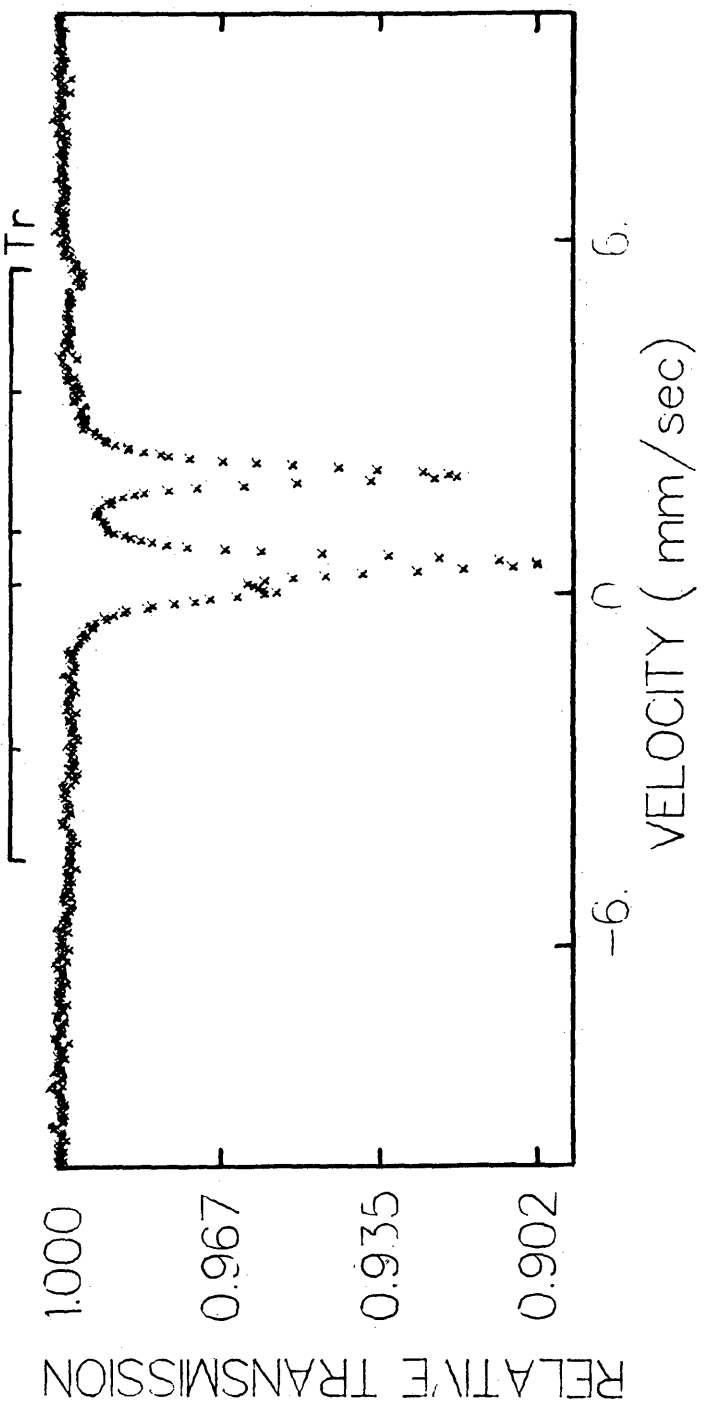

Figure 24. Paraho unretorted shale. Spectrum 289 run at 295K.

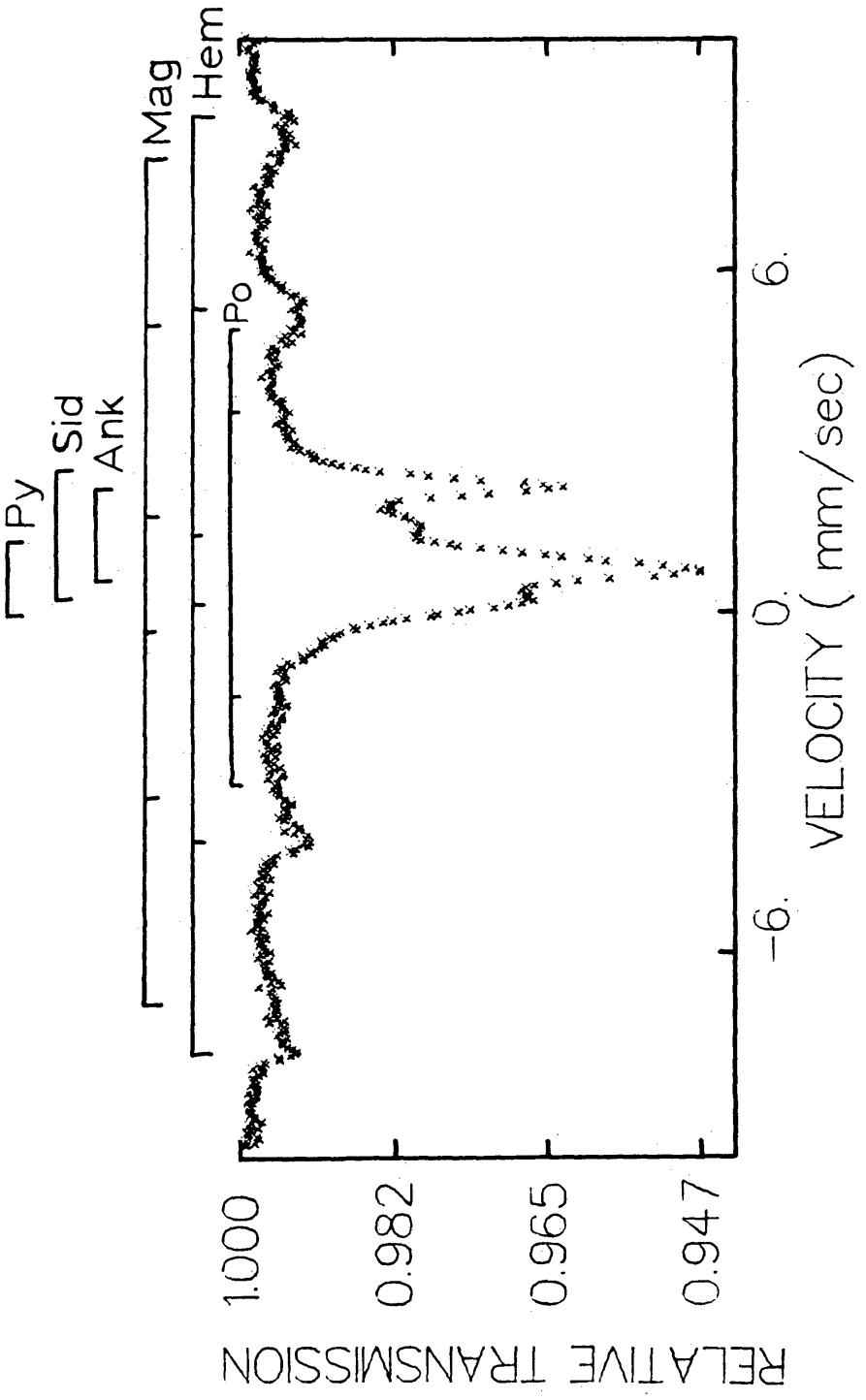

Figure 25. Paraho retorted shale. Spectrum 290 run at 295K.

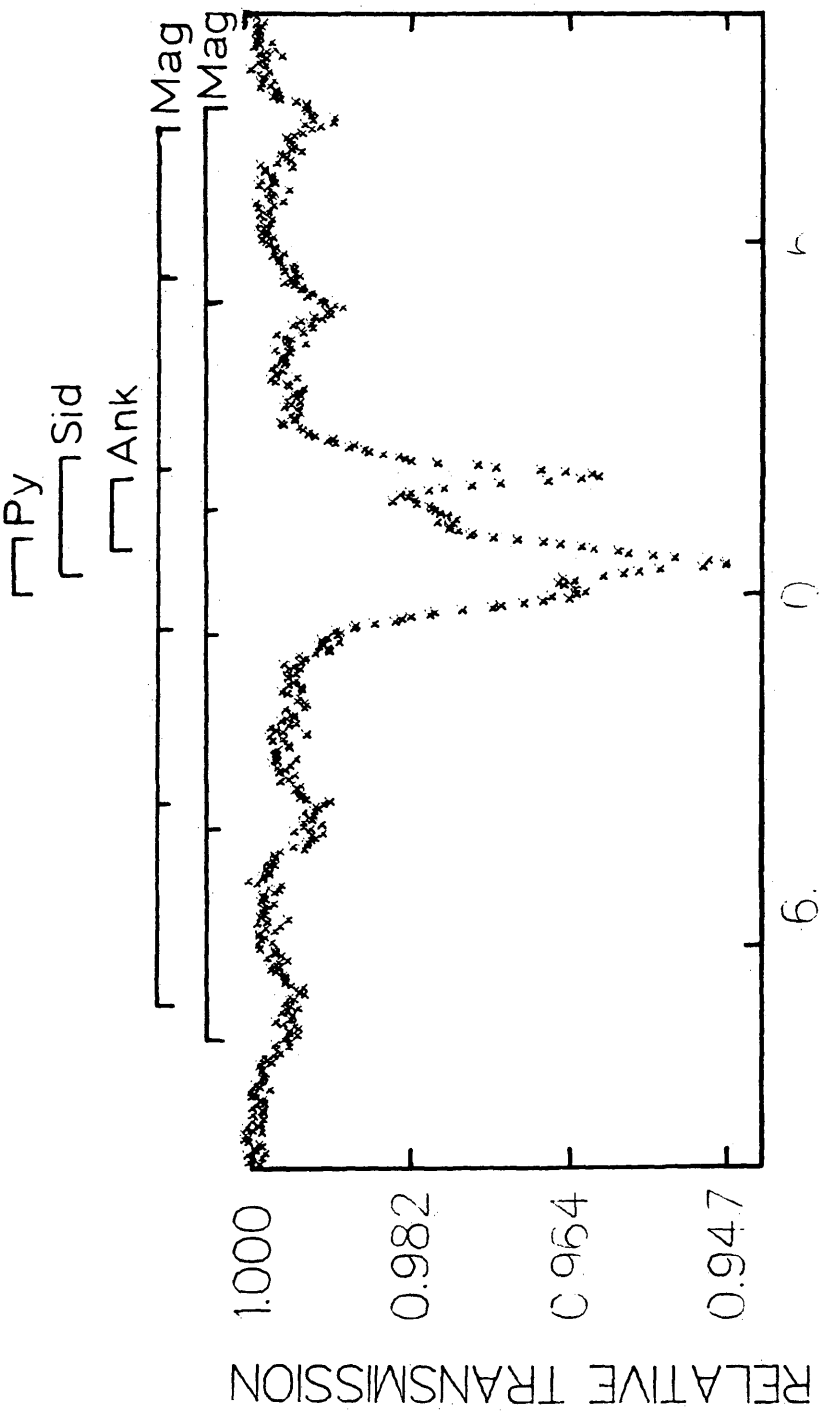

Figure 26. Dust from the Paraho baghouse. Spectrum 291 run at 295K.

Figure 27 Diagram of Mössbauer Spectrometer

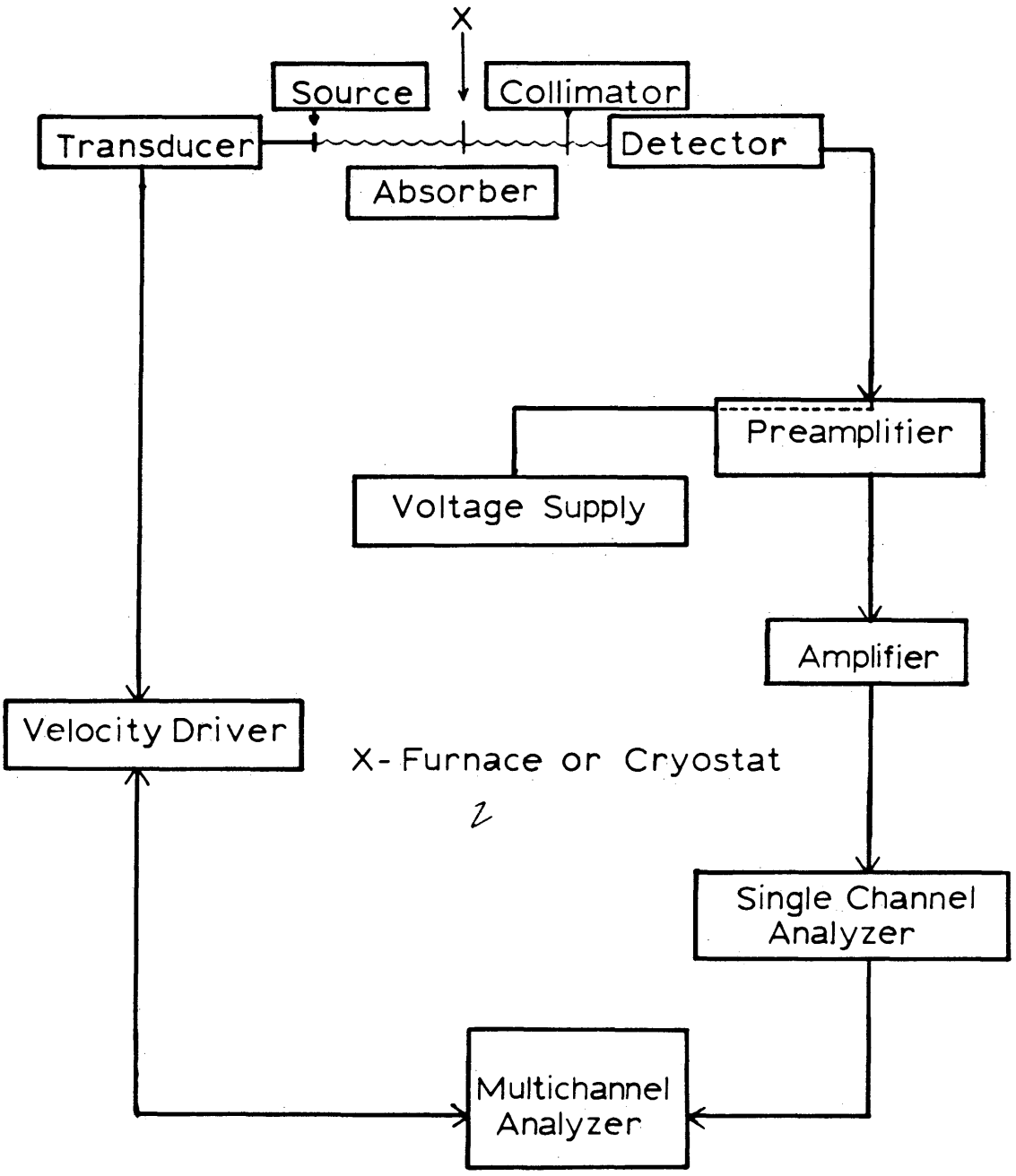

Figure 28. Cryostat Diagram

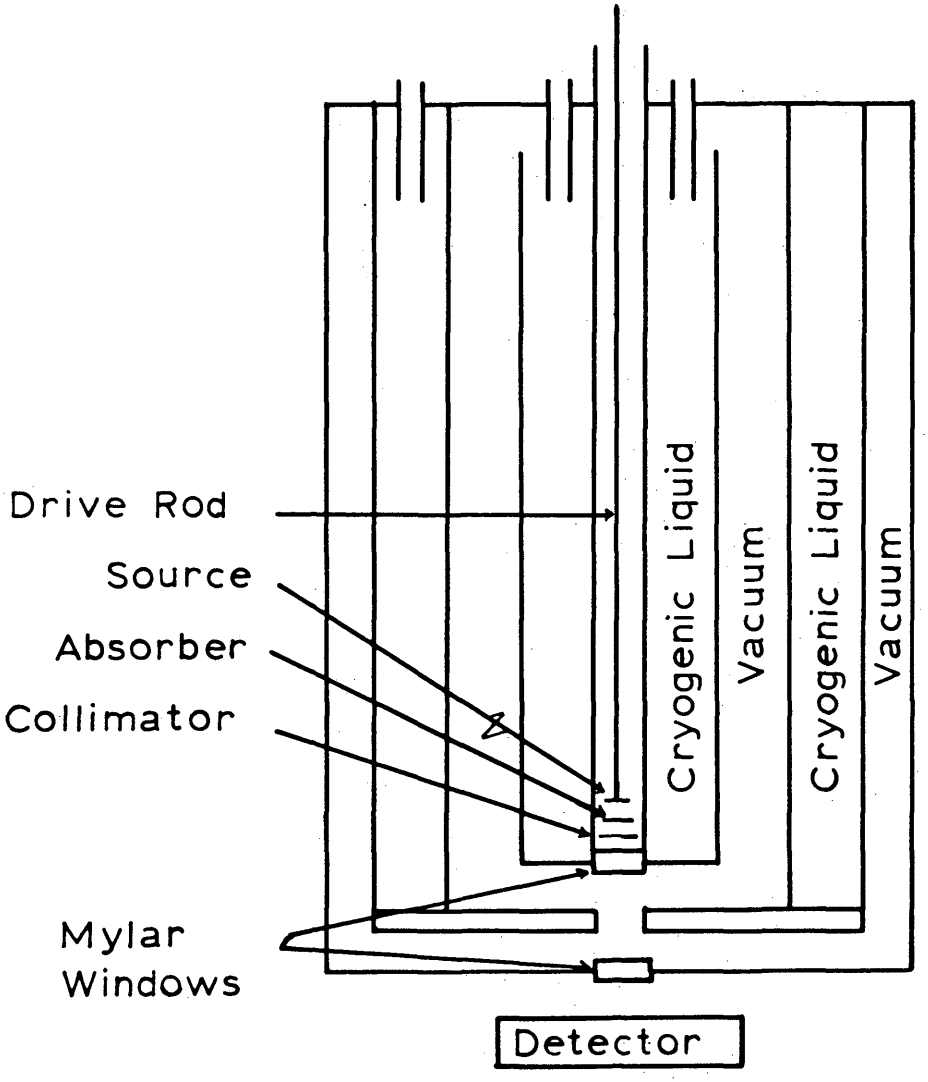

APPENDIX B DETERMINATION OF MÖSSBAUER PARAMETERS

The ability to use Mössbauer spectra qualitatively is directly related to the differences in the hyperfine interactions each compound exhibits. Hyperfine interactions yield an isomer shift (δ), quadrupole splitting (Δ), and magnetic splitting (H) In addition to these qualitative measurements, one other spectral parameter, half-height peak width, may be used to aid in fingerprinting the compounds being studied. The quantitative parameters include use of resonance areas, Lorentzian line shapes, effective thicknesses, and the recoilless fraction of each compound.

The isomer shift is a result of electrostatic interactions between the nucleus and electrons The chemical shift that is observed and reported from a Mössbauer spectrum is from both the isomer shift, plus a second order Döppler effect. The second order Döppler effect is usually neglected due to its small size compared to the isomer shift (Bancroft, (46)) The shifts reported in this paper are given with respect to the center of α-iron at ambient temperatures. Quadrupole splitting is observed when an inhomogeneous electric field acts on a non-spherical nucleus. The result of the split in energy levels is a doublet instead of a single peak in the resonance pattern. Magnetic splitting is a result of the interactions of an internally

created magnetic field and the nuclear dipole moment More detailed discussions on these parameters is available in Bancroft (46)

Prior to the determination of δ, Δ, and H, a calibration spectrum must be run. In this paper the calibration spectra were of ^{57}Fe enriched iron foil From the six line calibration spectrum, the center coordinate and calibration factor is determined. The iron foil resonance pattern is fitted with an algorithm using three pairs of Lorentzians The calibration factor (C) is determined by calculating the separation (S) in channels from the multichannel analyzer (MCA) between peaks 1 and 6, (S_{16}), 2 and 5, (S_{25}) and the innermost peaks 3 and 4, (S_{34}) These numbers are divided into the known velocities (47) for the splitting at that temperature. The three values are then averaged and given in the units mm/second-channel

$$C_{i:j} = \text{Velocity}_{i,j}(\text{mm/sec})/S_{i:j}(\text{channels})$$

The center coordinate (δ_0) is calculated by determining the average position of the six lines

The equations used in determining the isomer shift (δ), quadrupole splitting (Δ), magnetic splitting (H), and peak width at half height are given below

$$\delta = [P + {}^{Q}/_{2} + {}^{H'}/_{2} \quad \delta_0]C \qquad \text{mm/sec}$$

$$\Delta = QC \qquad \text{mm/sec}$$

$$H = 330H'C/10.6245 \qquad \text{KOe}$$

$$\tau = 2\tau'C \qquad \text{mm/sec}$$

P is the peak position in channels of the lowest velocity peak for quadrupole pairs and magnetic six line patterns. Q is the quadrupole splitting in channels H' is the magnetic splitting in channels τ' is the peak half-width at half height in channels

A special procedure is used for obtaining a calibration spectrum for an absorber in the cryostat. Figure 2 is a diagram of the cryostat. Either immediately prior or after running the low temperature spectrum another source is placed on top of the transducer followed by a metallic iron foil, graded collimator, and a proportional counter; the resonance pattern is then taken. The calibration is corrected for differences in the source's shift from α-iron and the change in shift due to the deviation from room temperature. Measurements taken in this lab show a shift of 0.133 mm/sec from α-iron at 300K for a ^{57}Co:Rh source at 76K compared to 300K. If the ^{57}Co:Rh source is at 76K and a calibration run is made using a ^{57}Co:Pd source at the opposite end of the

transducer, the shift from α-iron at 300K is 0.283 mm/sec. A calculation of the shift of the source from 76K to 6K was made based on the Debye model and found to be 0.009 mm/sec. Thus the shift of the ^{57}Co:Rh source from room temperature to 6K is 0.142 mm/sec. If both ^{57}Co:Pd and ^{57}Co:Rh sources are at room temperature, the differences in the shift with respect to α-iron are 0.177 mm/sec and 0.116 mm/sec, respectively.

APPENDIX C DETERMINATION OF EFFECTIVE THICKNESSES

Quantitative analysis using Mössbauer spectroscopy may be accomplished using several methods such as line intensity, resonance area, or effective thicknesses (48) Quantitative analysis was done in this study by using the ratios of the effective thickness values The effective thickness of an absorber is the number of ^{57}Fe atoms per cm^3 of the absorber and is related to the resonance area (A) calculation.

$$A = \frac{\pi}{2} \tau \frac{I}{N\infty} B \qquad \text{(mm/sec) of a single line}$$

B = background radiation correction

N∞ = off resonance counts

I = intensity of a single line (counts)

τ = line width of a single line

where B = 1/[1 1.04 (counts with a brass filter/counts without filter)] and is determined by measuring the count rate in the 14 4 KeV counting channel with and without a brass filter. The brass filter eliminates the contribution to the counts of the 14.4 KeV gamma rays.

The theoretical area under a resonance line is given by

$$A_{Theory} = \frac{\pi}{2} \tau_0 f_s K(T)$$

where

τ_0 natural line width of Fe (0.097 mm/sec)

f_s recoilless fraction of the source

0.889 for ^{57}Co:Rh at 6K$^{\Delta}$

0.88 for ^{57}Co:Rh at 76K[47]

0.78 for ^{57}Co:Rh at RT[47]

0.86 for ^{57}Co:Pd at 76K[47]

0.66 for ^{57}Co:Pd at RT[47]

([47]) Literature Values

(Δ) Calculated based on literature values plus an additional correction based on a Debye model

K(T) effective thickness function

if $A_{Theory} = A_{Experimental}$

$$K(T) = (I\tau B/N\infty \tau_0 f_s)$$

T is obtained from the K(T) vs T curve

$$T = \sigma n f_a t$$

where

σ = nuclear cross section of resonance

n = number of ^{57}Fe atoms/cm^3

f_a = recoilless fraction of the absorber

t = absorber thickness

Here we assume the recoilless fractions of the minerals studied are equal so that ratios of T will provide relative

fractions of the species present. The calculated T is for a given line in question; for a pattern that is either a quadrupole or magnetic spectrum, the following procedure is used.

For a magnetic spectrum: Powder absorber

The T of the left line of the spectrum multiplied by four will yield the total effective thickness. The ratio of the effective thicknesses associated with the six lines of a powdered random absorber will be 3:2:1:1:2:3.

For a quadrupole spectrum:

In a pattern that contains a quadrupole pair, the effective thickness of a single line of that spectrum is one half of the total effective thickness.

APPENDIX D DETERMINATION OF ERRORS

Uncertainties in the values given in Table 2 are given in terms of the uncertainty in the last digit. The uncertainty in each value is an estimate that is based on visual inspection of the computer decomposition and the uncertainties the computer algorithm yields based on counting statistics. A visual inspection of each converged fit is first made to determine if that particular fit best represents the experimental data. Following the choice of the best decomposition pattern, the parameters are calculated (See Appendix B). Uncertainty values are then attached to the calculated parameters with the aid of the computer algorithm. The program that was used in this study yields a value for each input parameter plus an error of the last approximation with a probability of 75 percent. This error is used with the subsequent equations to attach the error bars to each value. The error in the parameters is based on standard propagation of errors. For example:

$$\delta = [P + Q/2 + H'/2 \quad \delta_0]C \tag{1}$$

Since the error in δ_0 and C were generally small, their errors were neglected. The uncertainty in the parameters is given by λ.

$$\lambda\delta = \left[\left[\left(\frac{\partial\delta}{\delta P}\right)^2(\lambda P)^2 + \left(\frac{\partial\delta}{\partial Q}\right)^2(\lambda Q)^2 + \left(\frac{\partial\delta}{\delta H}\right)^2(\lambda H)^2 \right.\right.$$

$$\left.\left.\left(\frac{\partial\delta}{\partial\delta_0}\right)(\lambda\delta_0)^2\right]C^2\right]^{\frac{1}{2}} \qquad (2)$$

$$= \left[\left[(\lambda P)^2 + (\tfrac{1}{2})^2(\lambda Q)^2 + (\tfrac{1}{2})^2(\lambda H)^2\right]C^2\right]^{\frac{1}{2}} \qquad (3)$$

The errors in the other parameters were determined in a similar fashion. The results of this procedure performed on each equation yielded:

$$\lambda\Delta = \left[(\lambda Q)^2 C^2\right]^{\frac{1}{2}} \qquad (4)$$

$$\lambda H = \left[(330C/10.6245)^2(\lambda H')^2\right]^{\frac{1}{2}} \qquad (5)$$

$$\lambda\tau = \left[(2C)^2(\lambda\tau')^2\right]^{\frac{1}{2}} \qquad (6)$$

$$\lambda A = A\left[(\lambda I/I)^2 + (\lambda\tau'/\tau')^2\right]^{\frac{1}{2}} \qquad (7)$$

$$\lambda K(T) = K(T)\left[(\lambda I/I)^2 + (\lambda B/B)^2 + (\lambda\tau/\tau)^2\right]^{\frac{1}{2}} \qquad (8)$$

The term $(\lambda B/B)^2$ is neglected in equation 8 due to its small size.

APPENDIX E ADDITIONAL EXPERIMENTAL RESULTS

Table 3 contains the quantitative information on each species derived from each spectrum. Column one gives the sample and the conditions at which each was run, column two lists the spectrum number. Columns 3, 4, and 5 list the line width at half height of each species, resonance area for each species, and the effective thickness for each respectively. The sixth column gives the percentage of the mineral present based on the percent of the total effective thickness for the absorber. Experimental uncertainties in the last digit are given in parentheses

Table 3. ADDITIONAL MÖSSBAUER RESULTS

Sample	Spectrum	τ(mm/sec)	A(mm/sec)	T	% Fe	Mineral
OS-1	548	0.31(1)	0.138(3)	0.53(1)	42(3)	Pyrite
T=76K		0.31(1)	0.050(2)	0.26(1)	21(3)	Siderite
		0.31(1)	0.159(3)	0.45(1)	37(3)	Ankerite
OS-1	549	0.27(1)	0.105(2)	0.51(1)	39(3)	Pyrite
T-301K		0.27(1)	0.048(2)	0.61(1)	45(3)	Ankerite
		0.27(1)	0.087(2)	0.20(1)	16(3)	Siderite
SS-2	456	0.98(9)	0.028(3)	0.23(1)	18(4)	Pyrrhotite
T=298K		0.30(1)	0.092(5)	0.50(1)	40(5)	Ankerite
		0.30(1)	0.022(4)	0.13(1)	11(5)	Siderite
		0.30(1)	0.072(4)	0.40(1)	31(5)	Pyrite
Fischer Assay	552	0.61(6)	0.056(6)	0.48(6)	24(5)	Pyrrhotite
T=76K		0.7(1)	0.022(5)	0.20(6)	10(5)	Pyrrhotite
				0.95(6)	49(5)	Carbonate
				0.35	17(5)	Pyrite
Fischer Assay	550	0.48(9)	0.017(4)	0.17(2)	18(4)	Pyrrhotite
T=302K		0.52(8)	0.019(4)	0.19(2)	20(4)	Pyrrhotite
				0.36(4)	40(5)	Carbonate
				0.21(4)	22(5)	Pyrite
Raw 1B	588	0.29(1)	0.058(2)	0.25(2)	17(2)	Pyrite
T=76K		0.29(1)	0.176(2)	0.72(2)	48(2)	Ankerite
(center)		0.29(1)	0.072(2)	0.31(2)	21(2)	Siderite
		0.29(1)	0.058(2)	0.13(2)	9(2)	Illite
		0.22(9)	0.005(2)	0.07(2)	5(2)	Troilite

Table 3. Continued

Sample	Spectrum	τ(mm/sec)	A(mm/sec)	T	% Fe	Mineral
Raw 1B	269 & 603	0.26(1)	0.025(1)	0.23(3)	20(3)	Pyrite
T=298		0.26(1)	0.065(2)	0.56(3)	50(3)	Ankerite
		0.26(1)	0.021(8)	0.19(3)	17(3)	Siderite
		0.26(1)	0.008(4)	0.08(3)	7(3)	Illite
		0.5(2)	0.008(4)	0.07(3)	6(3)	Troilite
SOS-9	271	0.37(5)	0.017(2)	0.14(2)	12(4)	Pyrrhotite
T=298K		0.8(3)	0.018(5)	0.15(4)	13(4)	Pyrrhotite
		0.32(1)	0.070(5)	0.62(3)	55(4)	Ankerite
		0.32(1)	0.024(5)	0.12(4)	11(4)	Pyrite & Illite
		0.32(1)	0.019(5)	0.10(4)	9(4)	Siderite
SOS-7	267	0.43(2)	0.049(3)	0.48(1)	24(7)	Hematite
T=298K		1.7(1)	0.076(7)	0.72(2)	38(7)	Magnetite
		0.5(2)	0.04(1)	0.02(1)	17(7)	Carbonate
		0.6(3)	0.04(1)	0.02(1)	21(7)	Pyrite & Illite
SOS-10	378	0.44(4)	0.060(7)	0.48(6)	21(5)	Hematite
T=76K		0.82(4)	0.20(1)	1.50	67(5)	Magnetite
		0.7(1)	0.031(5)	0.15(5)	6(3)	Superparamagnetic
		0.6(1)	0.027(5)	0.13(5)	6(3)	Oxides
SOS-10	268	0.39(2)	0.044(2)	0.38(2)	20(5)	Hematite
T=295K		1.35(4)	0.133(5)	1.11(6)	59(5)	Magnetite
		0.96(7)	0.042(4)	0.20(2)	11(5)	Superparamagnetic
		0.96(8)	0.038(4)	0.19(2)	10(5)	Oxides

Table 3. Continued

Sample	Spectrum	τ(mm/sec)	A(mm/sec)	T	% Fe	Mineral
SOS-11B T=6K	575	0.50(4)	0.079(8)	0.54(4)	26(4)	Hematite
		0.85(4)	0.19(1)	1.27(5)	61(4)	Magnetite
		0.76(4)	0.037(6)	0.14(1)	7(4)	Superparamagnetic
		0.73(4)	0.035(5)	0.14(1)	6(4)	Oxides
SOS-11B T-76K	377	0.52(4)	0.075(7)	0.53(5)	27(3)	Hematite
		0.76(4)	0.154(9)	1.04(7)	53(3)	Magnetite
		0.72(6)	0.057(5)	0.22(2)	11(3)	Superparamagnetic
		0.59(5)	0.045(4)	0.18(2)	9(3)	Oxides
SOS-11B T=295K	266	0.40(2)	0.076(2)	0.39(2)	16(4)	Hematite
		1.53(5)	0.276(5)	1.34(6)	56(4)	Magnetite
		0.83(4)	0.062(7)	0.35(1)	15(4)	Superparamagnetic
		0.81(4)	0.057(7)	0.32(2)	13(4)	Oxides
SOS-11B T=491K	556	0.40(5)	0.015(2)	0.12(2)	16(3)	Hematite
		2.1(8)	0.07(2)	0.27(6)	37(8)	Magnetite
		0.64(4)	0.039(3)	0.16(2)	22(3)	Magnetite &
		0.66(5)	0.041(3)	0.18(2)	25(3)	Hematite
SOS-11B T=637K	557	0.40(6)	0.023(4)	0.11(4)	10(5)	Hematite
		0.59(3)	0.054(3)	0.27(1)	25(5)	Magnetite
		0.50(3)	0.045(3)	0.21(1)	19(5)	Magnetite &
		7.4(1.2)	0.11(2)	0.50(3)	46(6)	Hematite
SOS-11B T=773K	558	0.45(6)	0.010(2)	0.08(2)	12(10)	Hematite
		0.50(5)	0.027(3)	0.12(2)	19(10)	Magnetite
		0.57(5)	0.036(4)	0.16(2)	23(10)	Magnetite &
		2.6(4)	0.08(2)	0.33(9)	48(10)	Hematite

Table 3. Continued

Sample	Spectrum	τ(mm/sec)	A(mm/sec)	T	% Fe	Mineral
SOS-11B T=863K	559	0.89(5)	0.070(5)	0.30(2)	42(3)	Magnetite &
		1.07(4)	0.098(6)	0.41(3)	58(4)	Hematite
Paraho Unretorted Shale	Refer	RAW 1B				
Paraho Retorted	515	0.33(6)	0.013(4)	0.69(2)	25(5)	Hematite
	&	1.7(2)	0.11(2)	0.54(2)	19(5)	Magnetite
T = 298K	290	0.43(2)	0.094(5)	0.98(4)	36(10)	Carbonate
		0.43(2)	0.081(5)	0.44(9)	16(10)	Pyrite & Illite
		0.17(6)	0.013(5)	0.10	4(3)	Pyrrhotite
Paraho Baghouse Dust	291	0.28(2)	0.008(2)	0.067(1)	7(5)	Magnetite
		1.07(4)	0.047(3)	0.35(1)	40(5)	Magnetite
T = 298K		0.31(4)	0.023(3)	0.20(2)	23(9)	
		0.64(5)	0.015(3)	0.26(3)	30(10)	

APPENDIX F EXPERIMENTAL PROCEDURE

Each shale was ground and sieved to obtain a sample of -200 mesh. A one gram fraction is placed into a 2.54 cm diameter disk pelletizer. Sufficient pressure is applied to yield a pellet that held its shape. Subsequently each was covered with masking tape to increase the longevity The pressed pellets each had a thickness of about 1.5 mm.

The spectrum for each room temperature run is set up on the constant acceleration spectrometer (see Figure 27) in the following manner. Initially the pellet is placed in a lead lined holder adjacent to the source. A 0.25 inch graded collimator is placed up against the absorber. Lastly a lucite plug is screwed into the holder to alleviate any movement of the absorber and maintain a constant geometry throughout a run.

Several samples were run at conditions below ambient temperatures. To accomplish this, a commercial low temperature cryostat with a long drive rod is employed. Figure 28 is a diagram detailing the internal structure of the cryostat used. The source and absorber are mounted within the cryostat. Cryogenic liquid is transferred to a chamber adjacent to a helium filled heat transfer chamber in which the source and absorber are. Thus the source and absorber never come into direct contact with the cryogenic liquid.

In two retorted shales, a large fraction of the resonance was suspected to be due to superparamagnetic particles. To verify this point it became necessary to employ measurements at high temperatures. To accomplish this, a vacuum furnace was used and a special sample holder was fabricated of graphite. Figure 1 is a diagram of the fabricated cell The cell, containing an appropriate amount of material to yield results similar to a 2.54 cm diameter pellet, proved satisfactory for runs up to 863K. Figures 20 to 23 show the resonance patterns of SOS-11 from 491K to 863K.

Prior to analyzing each absorber, the γ-ray counting apparatus is adjusted to count only the 14 4KeV gamma rays. Lastly, the triangular wave form from the function generator is examined to determine if any wave deviations exist This procedure is critical for the low temperature runs as erratic movement of the long drive will create deviations in the triangular wave.

Each spectrum was run until it had adequate counts to enable computer deconvolution of the absorption pattern. The actual length of time required for each was dependent on the source strength, the amount of iron in each sample, and the temperature being used. As a general rule, liquid helium runs lasted a few hours, while the runs above that

temperature ran approximately one day.

Subsequent to the completion of each spectrum, the data was transferred to paper tape. The tape was then read into a DEC10 computer. Periodically velocity cali brations were obtained with metallic iron foils The absorption pattern for α-iron is well documented, with the splitting of lines known in terms of absolute velocities Thus it is possible to determine the various Mössbauer parameters based on a known standard.

To obtain maximum information from the resonance patterns, computer decomposition is employed. For these patterns, an algorithm based on a superposition of Lorentzian lines is used. A discussion of this procedure plus the determination of Mössbauer parameters and their associated errors may be found in Appendices B, C, and D.

APPENDIX G PREVIOUSLY REPORTED MÖSSBAUER PARAMETERS

Isomer shifts given with respect to α-Fe at 298K

	δ(mm/sec)	Δ(mm/sec)	H(KOe)	Reference
FeS (Troilite)	0.86	-0.28	310	28
Fe_7S_8	0.68	0.02	304	23
(Monoclinic	0.68	0.09	292	
Pyrrhotite)	0.66	0.06	251	
	0.66	0.07	227	
$Fe_{0.883}S$	0.668	-0.039	301	28
(Hexagonal	0.636	-0.021	259	
Pyrrhotite)	0.625	-0.069	231	
FeS_2 (Pyrite)	0.31	0.62		23
FeS_2 (Marcasite)	0.29	0.50		49
$FeCO_3$ (Siderite)	1.21	1.78		50
$Ca(Mg,Fe)(CO_3)_2$ (Ankerite)	1.20	1.50		50
Illite	1.12	2.62		23
Fe_2O_3 (Hematite)	0.37	-0.10	515	31
Fe_3O_4 (Magnetite)	0.67	0.0	463	51
	0.31	0.0	498	